Contents

1 Introduction and motivation

Satellite trajectory models for space-based SAR systems, such as the parabolic or hyperbolic range models, need to be improved to handle high-resolution SAR imaging modes with long synthetic apertures. For instance, such is the case for the staring spotlight mode on TerraSAR/TanDEM-X. Several authors, such as those in [1–3], have derived methods to achieve improved SAR processing methods for very high-resolution systems. Reference [1] provides an excellent description of the approach most likely taken with 0.19cm resolution (azimuth) of the staring spotlight mode on TerraSAR/TanDEM-X.

In addition to the new high-resolution spotlight modes, developments in multi-channel SAR systems promise the ability to also create high-resolution imagery, [4]. This document presents a first-principles-based model for the multi-channel SAR mode that extends the work of, for instance, [4, 5], thereby developing the theory to process very high-resolution SAR imagery from multi-channel configurations.

1.1 Organization

The document is structured as follows: the first section outlines limitations inherent with a circular orbit assumption (even locally) demonstrating that not only is the curvature of the orbit an issue for high resolution SAR, but so also the torsion (curvature and torsion to be defined in Section 4). The section shows that uniform slow-time sampling does not, in general, equate to uniform azimuth spatial sampling. These results are demonstrated with real Sentinel-1 orbit data.

The next section reviews some introductory concepts from differential geometry and applies the thoery to the curve of a SAR satellite in an Earth-Centred, Earth-Fixed coordinate system. The adoption of the differential geometry approach introduces an arclength parameterization of the SAR orbit which provides a natural setting for SAR imaging. This section is followed by a description of how physical parameters such as the state vectors or the accelerations (time based) transform into differential geometry parameters such as the curvature and torsion.

Sections 5 and 6 extend the work reported in [4, 5] by applying the differential geometry approach to SAR imaging, specifically to a SAR antenna that contains a spatial offset baseline. The inclusion of the baseline sets the stage for multi-channel processing. The next section transforms the signal into the wavenumber domain leading to Section 7.2 which examines the transformation of the antenna pattern in the wavenumber domain. Section 7.2 shows, importantly, that the individual data signals from each channel can be described by a commmon componenent that does not depend on the channel baseline or channel azimuth antenna pattern, and a varying component that depends only on the arclength parameter (there is only a negligeable range dependence on the multi-channel signal processing). This greatly simplifies and accelerates the multi-channel signal processing.

The next section applies an already published multi-channel signal processing approach to the developed signal. This is followed by a demonstration of the entire approach to the super resolution approach.

The authors know no better language than mathematics to describe the new parameterizations of the SAR signal and to describe this signal in different domains. That stated, we repeatedly strive to minimize the amount of mathematics and to phrase the derivations and interpretations of the results using physical quantities and concepts. In an attempt to make the document more readable, mathematical derivations have been placed into an appendix

with only the results of the mathematical investigations reported in the main text.

2 A closer look at SAR from an orbiting satellite

A quick review of data from currently orbiting systems shows that, when viewed from an Earth-Centered, Earth-Fixed (ECEF) coordinate system, Low Earth Orbit (LEO) SAR satellites do not travel with a constant velocity, nor do they orbit at a constant range. These satellites experience constant changes in the amplitudes of their accelerations, not only because they follow elliptical orbits, but also because of variations in the Earth's gravitational field. This is true not only globally, but also locally and means that as one attempts to produce higher and higher resolution imagery, one runs into limitations in SAR signal processing algorithms based upon circular orbits. Depending on the orbit, uniform slow-time sampling does not equate to uniform spatial sampling. This poses a potential problem for multi-channel SAR imaging systems that in some fashion depend upon uniform spatial samples. The following text expands on these issues.

2.1 A closer examination of locally circular orbits

Figures 1 and 2 illustrate real data extracted from precise orbit ephemerides computed for Sentinel-1 and sourced from https://qc.sentinel1.eo.esa.int/aux_poeorb/. One sees that over a couple of seconds, the radius of the orbit has changed by several meters. As well, the velocity has changed by a tenth of a meter per second. These quantities are rather large when compared to the wavelength of (in this case for Sentinel-1) about 0.05 m.

For the synthetic aperture lengths employed by Sentinel-1 and most commercial systems (RADARSAT-2, RCM, Palsar), the deviations described are not critical to image formation. The non-constant nature of the target range, and of the ECEF velocity, can be hidden by algorithms that, instead of calcuating from first principles, numerically estimate the required SAR processing parameters.

This work seeks to provide first-principles-based accounting for how to compute the SAR processing parameters. Such information could help with

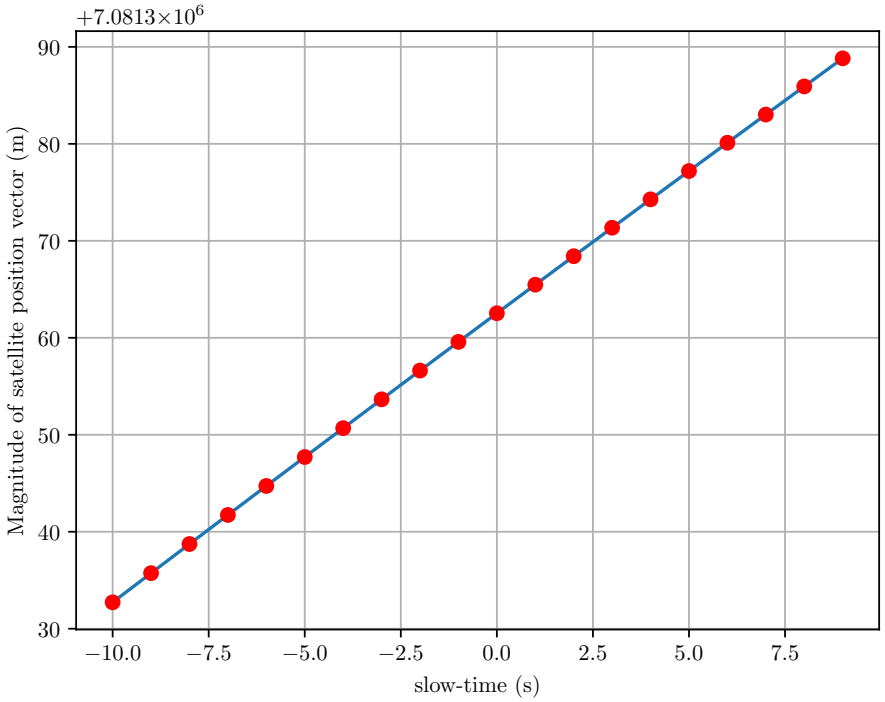

Figure 1: Non-constant satellite radius in the ECEF coordinate system. Data extracted from Sentinel-1 Precise Orbit Ephemerides. https://qc.sentinel1.eo.esa.int/aux_poeorb/

on-board SAR processing shemes where the data required to numerically calculate the required parameters is more difficult to obtain.

The document uses the theory of the differential goemetry of curves in three dimensions as a mathematical basis, and applies a physical model based upon the spherical harmonic model of the Earth's gravitational potential. Although a review of differential geometry is provided herein, a higly recommended reference can be found in http://homepages.math.uic.edu/~jwood/analysis/Curvegeomrev.pdf. Equally, a higly recommended reference for application of the spherical harmonic model to satellite motion can be found at https://www.hindawi.com/journals/ijap/2014/903026/.

As a final comment, note that calculations for the satellite positions have been made using the egm96 spherical harmonic expansions available at https://nasa.site.egm96 through custom python code.

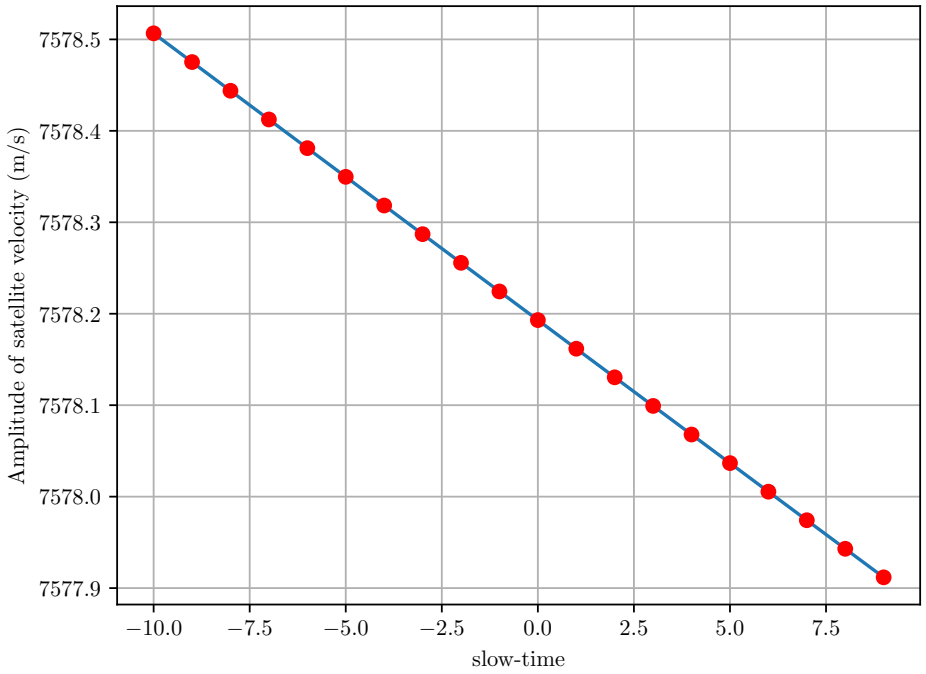

Figure 2: Non-constant satellite velocity in the ECEF coordinate system. Data extracted from Sentinel-1 Precise Orbit Ephemerides. https://qc.sentinel1.eo.esa.int/aux_poeorb/

2.2 Non-linearity between arclength and time

The previous section presented real data showing that target range and satellite velocity do not remain constant over time. This section derives a relationship between arclength and slow-time for the purpose of demonstrating that they are, in general, not linearly related. The actual synthetic aperture that forms a beam is derived from a set of points that are not uniformly spatially spaced.

To begin the derivation, denote the parameterized satellite position vector as $\mathbf{c}_s(s)$, where the parameter s denotes arc length. This position vector defines a curve in three dimensions. The relation between arclength and time t is defined as

$$s = \int_0^t |\dot{\mathbf{c}}_t(\xi)| \mathrm{d}\xi. \tag{1}$$

The dot notation, $\dot{\mathbf{c}}_t(\xi)$, indicates the derivative with respect to time, so the above simply states that arc length is the integration of the amplitude of the intantanous satellite velocity over time[1]. Rather than computing the exact integral, an expansion to third order suffices for most applicaitons. By applying the vector calculus relations outlined in Appendix A, one finds that

$$\frac{\mathrm{d}s}{\mathrm{d}t} = |\dot{\mathbf{c}}_t(t)| \tag{2}$$

$$\frac{\mathrm{d}^2 s}{\mathrm{d}t^2} = \hat{\dot{\mathbf{c}}}_t^{\dagger}(t)\ddot{\mathbf{c}}_t(t) \tag{3}$$

$$\frac{\mathrm{d}^3 s}{\mathrm{d}t^3} = \frac{\ddot{\mathbf{c}}_t{}^{\dagger}(t)\mathbf{P}_{\dot{\mathbf{c}}_t(t)}\ddot{\mathbf{c}}_t(t)}{|\dot{\mathbf{c}}_t(t)|} + \hat{\dot{\mathbf{c}}}_t^{\dagger}(t)\dddot{\mathbf{c}}_t(t). \tag{4}$$

In the above, the projection operator $\mathbf{P}_{\mathbf{y}}$ applied on the vector $\mathbf{x}$ extracts the component of $\mathbf{x}$ that is perpendicular to the vector $\mathbf{y}$. The derivatives can be used to expand the expression for arclength around $t = 0$:

$$s \approx \frac{t}{1!}|\dot{\mathbf{c}}_t(0)| + \frac{t^2}{2!}\hat{\dot{\mathbf{c}}}_t^{\dagger}(0)\ddot{\mathbf{c}}_t(0) + \frac{t^3}{3!}\left[\frac{\ddot{\mathbf{c}}_t{}^{\dagger}(0)\mathbf{P}_{\dot{\mathbf{c}}_t(0)}\ddot{\mathbf{c}}_t(0)}{|\dot{\mathbf{c}}_t(0)|} + \hat{\dot{\mathbf{c}}}_t^{\dagger}(0)\dddot{\mathbf{c}}_t(0)\right]. \tag{5}$$

Disregarding the third order term in t, consideration of the above reveals that s and t are only proportional when the orbit is such that the velocity vector

[1] by definition, $\dot{\mathbf{c}}_t(t)$ is the satellite velocity vector, $\ddot{\mathbf{c}}_t(t)$ is the satellite acceleration vector, e.t.c.

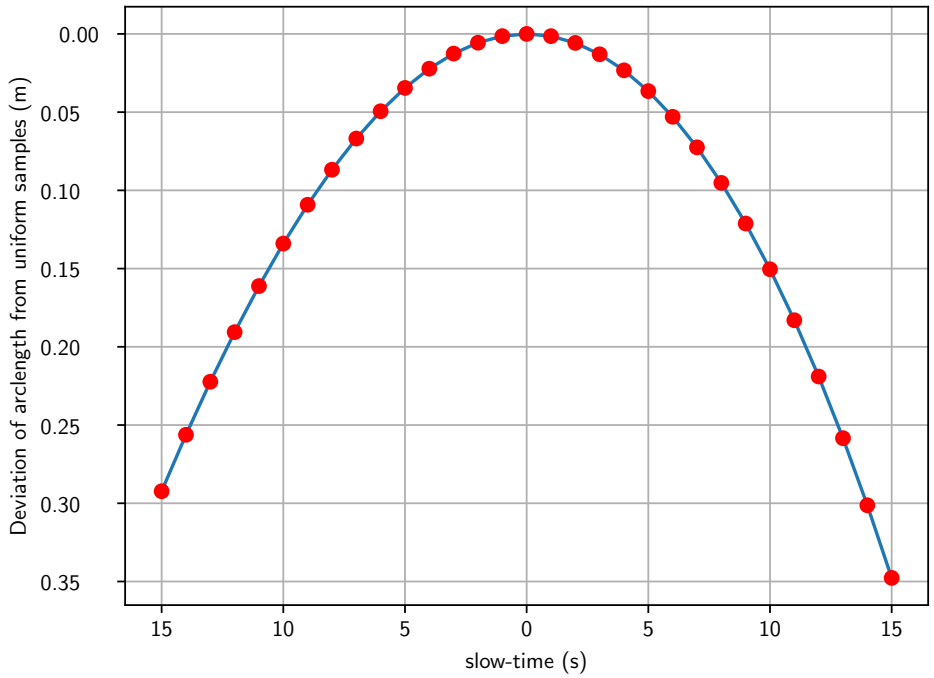

Figure 3: Deviation of arclength from uniform samples in meters as a function of slow-time. That is, the arclengths deviates from from a linear realtionship with slow-time by the amount on the y-axis. Data extracted from Sentinel-1 Precise Orbit Ephemerides. https://qc.sentinel1.eo.esa.int/aux_poeorb/

is perpendicular to the acceleration vector $\hat{\mathbf{c}}_t^{\dagger}(t)\ddot{\mathbf{c}}_t(t) = 0$, which, in general, is not the case. And if time and position are not proportional, then any synthetic aperture processing algorithm derived from uniform time samples is only approximately correct because the spatial samples are non-uniform. This is akin to using a phased-array radar with non-uniformly distributed array phase-centres.

Figure 3 shows how arc length shrinks as a function of slow-time for real Sentinel-1 measurements. Only in the region of ± 1 second is the arclength difference small enough to be ignored (0.009 m). By the time one arrives at two seconds, the arclength is $0.03m$ shorter than expected from a linear

realtionship between time and arclength, and in this region, one is already approaching the C- and X-band wavelengths.

From a physical point of view, this means that with a uniform PRF, spatial samples become increasingly non-uniform as the synthetic aperture length increases which, in turn, complicates Doppler domain multi-channel image processing since these generally rely upon uniform sampling.

2.3 Arclength parameterization approach

A potential solution, and the recommendation of this document, is to design satellite radar systems that vary their PRF in order to maintain uniform spatial sampling. This could possibly be achieved by triggering pulse transmission based upon a device that not only measures arclength through inertial measurements but also adjusts for non-inertial earth rotation effects.

Most space-based SAR literature develops the signal using fast-time, slow-time coordinates, but there are advantages to approaching the development using arclength instead of slow-time. These include a simplified (in the opinion of the authors) derivation, an approach that inherently assumes uniform spatial sampling and, perhaps most importantly, a means to apply a first-principles-based approach based upon the highly accurate gravitational model provided by the NGA/NIMA spherical harmonic libraries known as egm96 or egm2008.

After a quick accounting for the notation used in this document, Section 4 provides a brief review of some elementary differential geometry concepts and shows how they relate to physical quantities associated with SAR imaging. This is followed by Section 5 which implements these concepts and derives the SAR signal as a function of range wavenumber and arclength wavenumber.

3 Notation

This document describes the SAR collection geometry with two primary variables: these are the range, r, which represents the across-track or fast-time dimension ($\tau = 2r/c$) and s which defines arclength in the along-track dimension. In this chapter, we adopt a two-symbol notation for the measured scalar signal, see Table 1; the first symbol corresponds to the domain of the r variable while the second indicates the domain of the s variable. For aesthetic reasons, we represent the measured vector and matrix signals using a single symbol; vectors, with lowercase bold, $\mathbf{s}(k_r, k_s)$, and matrices, with uppercase bold, $\mathbf{S}(k_r, k_s)$. Also note that the symbol $\cdot^\dagger$ is used to denote the complex conjugate of a vector which, for a real-valued vector or matrix, reduces to the regular transpose operation. The magnitude of a vector is denoted with italicised text; for instance, $|\mathbf{r}(s, \mathbf{x})| = r(s)$. The summation without specifying limits, $\sum_l$, denotes summation over all l from $-\infty$ to ∞. Similarly an integration without limits indicates integration over an infinite domain.

3.1 The multi-channel signal as a superposition of vectors

Without loss of generality, one may consider the measured signals in the 2-D spatial frequency domain. In this domain, if one has measurements from N (possibly different) two-way antennas, the measured signal may be represented as a vector, $\mathbf{z}(k_r, k_s)$, with each element corresponding to the measurement from each of the different two-way antennas in the presence of

	Range	**Azimuth**
$ss_n(\tau, s)$	fast-time (s)	arclength (m)
$Ss_n(\omega, s)$	angular-frequency (rad/s)	arclength (m)
$\mathcal{S}s_n(k_r, s)$	wavenumber (rad/m)	arclength (m)
$\mathcal{SS}_n(k_r, k_s)$	wavenumber (rad/m)	wavenumber (rad/m)

Table 1: Notation for the scalar signal in various domains. The subscript denotes the n^{th} channel.

additive white Gaussian noise:

$$\begin{aligned}\mathbf{z}(k_r,k_s) &= \sum_l \begin{bmatrix} \mathcal{SS}_1(k_r,k_s+lk_{s_p}) \\ \mathcal{SS}_2(k_r,k_s+lk_{s_p}) \\ \vdots \\ \mathcal{SS}_N(k_r,k_s+lk_{s_p}) \end{bmatrix} + \mathbf{n}(k_r,k_s) \\ &= \sum_l \mathbf{s}(k_r,k_s+lk_{s_p}) + \mathbf{n}(k_r,k_s)\end{aligned} \tag{6}$$

where $\mathbf{n}(k_r,k_s)$ is additive white noise.

In the above, k_r is a wavenumber that corresponds to the fast-time or range dimension related to the frequency of the signal via $k_r = 2\omega/c$ where ω is the radial frequency (in radians per second) of the signal and c is the speed of light. Correspondingly, k_s is a wavenumber corresponding to the slow-time-related arclength parameter.

4 Differential geometry of curves in 3D

This section reviews material abundant in published literature; for instance, see http://homepages.math.uic.edu/~jwood/analysis/Curvegeomrev.pdf for a highly recommended introduction. While the material presented is complete for understanding the application to SAR imaging, it represents only a small tip of the theory and is by no means original - even common differential geometry notation has been maintained.

In this short section all the required tools to develop the SAR satellite signal model are presented.

For a curve in three dimensions given by $\mathbf{c}_s(s)$, the tangent vector is given by $\mathbf{T}(s) = \mathbf{c}_s'(s)$. Because of the arclength parameterisation, $\mathbf{T}(s)$ is a unit vector and $\mathbf{T}(s)\cdot\mathbf{T}'(s) = 0$. The **curvature** is defined as $\kappa(s) = |\mathbf{T}'(s)|$. Define the unit vector

$$\mathbf{N}(s) = \mathbf{T}'(s)/\kappa(s). \tag{7}$$

The binormal vector $\mathbf{B}(s)$ is defined as $\mathbf{B}(s) = \mathbf{T}(s)\times\mathbf{N}(s)$. The vectors $\mathbf{T}(s),\mathbf{N}(s),\mathbf{B}(s)$ form an orthonormal basis.

Since $\mathbf{T}(s)\cdot\mathbf{N}(s) = 0$,

$$\begin{aligned}\mathbf{T}(s)\cdot\mathbf{N}'(s) &= -\mathbf{T}'(s)\cdot\mathbf{N}(s) \\ &= -\kappa(s)\end{aligned} \tag{8}$$

Define the **torsion** as $\tau(s) = \mathbf{N}'(s) \cdot \mathbf{B}(s)$. Then, by multiplying $\mathbf{N}'(s) = a_T\mathbf{T}(s) + a_N\mathbf{N}(s) + a_B\mathbf{B}(s)$ successively by $\mathbf{T}(s), \mathbf{N}(s), \mathbf{B}(s)$, one finds that

$$\mathbf{N}'(s) = -\kappa(s)\mathbf{T}(s) + \tau(s)\mathbf{B}(s) \tag{9}$$

Finally, one finds that

$$\begin{aligned}\mathbf{B}'(s) &= \mathbf{T}'(s) \times \mathbf{N}(s) + \mathbf{T}(s) \times \mathbf{N}'(s) \\ &= \kappa(s)\mathbf{N}(s) \times \mathbf{N}(s) + \mathbf{T}(s) \times [-\kappa(s)\mathbf{T}(s) + \tau(s)\mathbf{B}(s)] \\ &= -\tau(s)\mathbf{N}(s)\end{aligned} \tag{10}$$

The previous few expressions lead to the Frenet-Serret equation

$$\begin{bmatrix}\mathbf{T}'(s) \\ \mathbf{N}'(s) \\ \mathbf{B}'(s)\end{bmatrix} = \begin{bmatrix} & \kappa(s) & \\ -\kappa(s) & & \tau(s) \\ & -\tau(s) & \end{bmatrix} \begin{bmatrix}\mathbf{T}(s) \\ \mathbf{N}(s) \\ \mathbf{B}(s)\end{bmatrix}. \tag{11}$$

The Frenet-Serret equations will be used in numerous places throughout this document to derive quantities related to the SAR signal model.

One observes that

$$\begin{aligned}\mathbf{c}_s'(s) &= \mathbf{T}(s) \\ \mathbf{c}_s''(s) &= \mathbf{T}'(s) = \kappa(s)\mathbf{N}(s) \\ \mathbf{c}_s'''(s) &= \kappa'(s)\mathbf{N}(s) + \kappa(s)\mathbf{N}'(s) \\ &= \kappa'(s)\mathbf{N}(s) - \kappa^2(s)\mathbf{T}(s) + \kappa(s)\tau(s)\mathbf{B}(s)\end{aligned} \tag{12}$$

Thus, a third order polynomial approximation to the satellite orbit can be expressed as

$$\begin{aligned}\mathbf{c}_s(s) \approx \mathbf{c}_p(s) = \mathbf{c}_s(s_0) + (s-s_0)\mathbf{T}(s_0) + \frac{(s-s_0)^2}{2!}\kappa(s_0)\mathbf{N}(s_0) \\ + \frac{(s-s_0)^3}{3!}[\kappa'(s_0)\mathbf{N}(s_0) - \kappa^2(s_0)\mathbf{T}(s_0) + \kappa(s_0)\tau(s_0)\mathbf{B}(s_0)]\end{aligned} \tag{13}$$

To make the notation more compact, we introduce $\mathbf{T}_0$, $\mathbf{N}_0$, $\mathbf{B}_0$, κ_0, $\dot{\kappa}_0$, τ_0 as all the respective functions evaluated at some suitably chosen s_0.

$$\begin{aligned}\mathbf{c}_p(s) = \mathbf{c}_s(s_0) + (s-s_0)\mathbf{T}_0 + \frac{(s-s_0)^2}{2}\kappa_0\mathbf{N}_0 \\ + \frac{(s-s_0)^3}{6}[-\kappa_0^2\mathbf{T}_0 + \dot{\kappa}_0\mathbf{N}_0 + \kappa_0\tau_0\mathbf{B}_0]\end{aligned} \tag{14}$$

4.1 Calculation of differential geometry parameters from position, velocity and acceleration

Computation of pysical spacecraft parameters requires relating arclength to time. This section derives the relations between slow time and arclength using relations derived in Appendix A. In the text below, the satellite curve as a function of arclength, $\mathbf{c}_s(s)$, is related to the same curve as a function of slow time $\mathbf{c}_t(t)$. While $\mathbf{c}_s'(s)$ denotes the derivative of the curve with respect to arclength, $\dot{\mathbf{c}}_t(t)$ denotes the derivative of the curve with respect to slow time.

Since

$$\mathbf{T}(s) = \frac{\mathrm{d}\mathbf{c}_s}{\mathrm{d}s} = \frac{\mathrm{d}\mathbf{c}_t(t)}{\mathrm{d}t}\frac{\mathrm{d}t}{\mathrm{d}s} = \frac{1}{|\dot{\mathbf{c}}_t(t)|}\dot{\mathbf{c}}_t(t) = \hat{\dot{\mathbf{c}}}_t(t). \tag{15}$$

In the above and in the expressions below, the equation on the left, a function of s is related to an expression on the right, a function of t, under the relation that t is a function of s, i.e. $t = t(s)$. The tangent vector, $\mathbf{T}(s)$, is just the unit velocity vector. With $k(s) = |\mathbf{T}'(s)|$, and with the aid of Appendix A, one computes

$$\frac{\mathrm{d}\mathbf{T}(s)}{\mathrm{d}s} = \frac{1}{|\dot{\mathbf{c}}_t(t)|}\frac{\mathrm{d}\hat{\dot{\mathbf{c}}}_t(t)}{\mathrm{d}t} = \frac{\mathbf{P}_{\dot{\mathbf{c}}_t(t)}\ddot{\mathbf{c}}_t(t)}{|\dot{\mathbf{c}}_t(t)|^2} \tag{16}$$

so that

$$k(s) = \frac{|\mathbf{P}_{\dot{\mathbf{c}}_t(t)}\ddot{\mathbf{c}}_t(t)|}{|\dot{\mathbf{c}}_t(t)|^2}. \tag{17}$$

Recall that $\mathbf{N}(s)$ is defined as the unit vector in the direction of $\mathbf{T}'(s)$. With the previous expression, one finds that

$$\mathbf{N}(s) = \frac{\mathbf{P}_{\dot{\mathbf{c}}_t(t)}\ddot{\mathbf{c}}_t(t)}{|\mathbf{P}_{\dot{\mathbf{c}}_t(t)}\ddot{\mathbf{c}}_t(t)|} = \hat{\mathbf{w}}(t), \tag{18}$$

with $\mathbf{w}(t) = \mathbf{P}_{\dot{\mathbf{c}}_t(t)}\ddot{\mathbf{c}}_t(t)$. This means that

$$\mathbf{N}'(s) = \frac{1}{|\dot{\mathbf{c}}_t(t)|}\frac{\mathrm{d}}{\mathrm{d}t}\hat{\mathbf{w}}(t) = \frac{1}{|\dot{\mathbf{c}}_t(t)|}\frac{\mathbf{P}_{\mathbf{w}}(t)\dot{\mathbf{w}}(t)}{|\mathbf{w}(t)|}. \tag{19}$$

It is also possible to compute that

$$\begin{aligned}\dot{\mathbf{w}}(t) &= \frac{\mathrm{d}\mathbf{P}_{\dot{\mathbf{c}}_t(t)}\ddot{\mathbf{c}}_t(t)}{\mathrm{d}t} \\ &= -\frac{1}{|\dot{\mathbf{c}}_t(t)|}\left[\mathbf{P}_{\dot{\mathbf{c}}_t(t)}\ddot{\mathbf{c}}_t(t)\hat{\dot{\mathbf{c}}}_t^T(t) + \hat{\dot{\mathbf{c}}}_t(t)\ddot{\mathbf{c}}_t{}^T(t)\mathbf{P}_{\dot{\mathbf{c}}_t(t)}\right]\ddot{\mathbf{c}}_t(t) + \mathbf{P}_{\dot{\mathbf{c}}_t(t)}\dddot{\mathbf{c}}_t(t).\end{aligned} \tag{20}$$

Thus

$$\mathbf{N}'(s) = \frac{1}{|\dot{\mathbf{c}}_t(t)|}\frac{\mathbf{P}_{\mathbf{w(t)}}}{|\mathbf{w}(t)|}\left[-\frac{1}{|\dot{\mathbf{c}}_t(t)|}\left[\mathbf{P}_{\dot{\mathbf{c}}_t(t)}\ddot{\mathbf{c}}_t(t)\hat{\mathbf{c}}_t^T(t) + \hat{\mathbf{c}}_t(t)\ddot{\mathbf{c}}_t{}^T(t)\mathbf{P}_{\dot{\mathbf{c}}_t(t)}\right]\ddot{\mathbf{c}}_t(t) + \mathbf{P}_{\dot{\mathbf{c}}_t(t)}\dddot{\mathbf{c}}_t(t)\right] \tag{21}$$

These expressions permit calculation of the tangent, normal and binormal vectors, the curvature and the torsion.

4.2 Demonstration of accuracy of the model

With the above relations, Figure 4 plots the satellite position using (14) and compares the result with the numerical integration of the satellite position. Section 9 explains how numerical integration of the satellite differential equations of motion is achieved and futher demonstrates how the numerically integrated results are accurate to within a few millimeters over an integration time of plus or minus forty seconds. The satellite position derived through numerical integration thus provides a highly accurate reference against which to test (14). Figure 4 shows that using (14) over a period of plus/minus ten seconds does not introduce any error greater than 5 mm in the satellite position.

Equation (14) thus provides a highly accurate and readily computable mathematical function to express the satellite position during a period of twenty seconds.

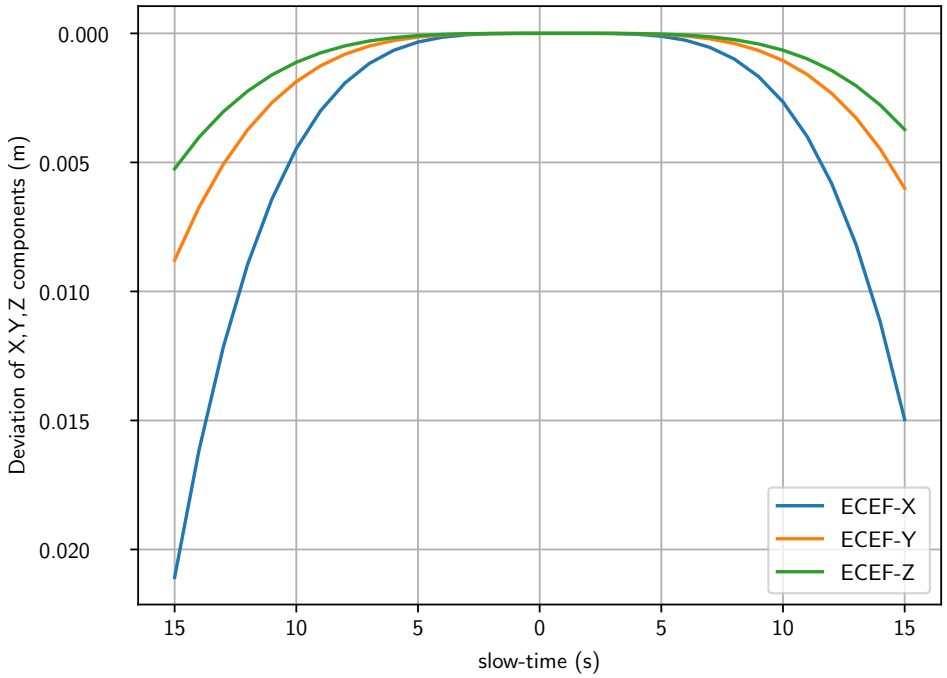

Figure 4: Difference between application of (14) and numerical integration of the differential equation of satellite satellite motion. State vector sourced from https://qc.sentinel1.eo.esa.int/aux_poeorb/.

5 Arclength-paremterized range function

As the range history plays a critical role in the development of the SAR signal model, this section relates the previously developed arclength parameterized satellite curve to the range history of a scatterer.

For a scatterer at point $\mathbf{x}$, there is a value, $s_{\mathbf{x}}$, such that $\mathbf{c}_p(s_{\mathbf{x}}) - \mathbf{x}$ is perpendicular to $\mathbf{c}_p'(s_{\mathbf{x}})$. That is, there exists a broadside arclength parameter[2]. Further, $\mathbf{x}$ can be completely determined by

$$\mathbf{x} = \mathbf{c}_p(s_{\mathbf{x}}) + r\cos\phi\mathbf{N}(s_{\mathbf{x}}) + r\sin\phi\mathbf{B}(s_{\mathbf{x}}), \tag{22}$$

where $r = |\mathbf{c}_p(s_{\mathbf{x}}) - \mathbf{x}|$ and $r\cos\phi = [\mathbf{x} - \mathbf{c}_p(s_{\mathbf{x}})] \cdot \mathbf{N}(s_{\mathbf{x}})$. One notes that ϕ relates to the depression angle of observation.

One can define the "nearest"-range vector associated to the point $\mathbf{x}$ as

$$\mathbf{r}(s_{\mathbf{x}}, \mathbf{x}) = r\cos\phi\mathbf{N}(s_{\mathbf{x}}) + r\sin\phi\mathbf{B}(s_{\mathbf{x}}). \tag{23}$$

Appendix C uses (14) and the above coordinate transformation $\mathbf{x} \to (r, s_{\mathbf{x}}, \phi)$ to produce the highly-accurate approximation that

$$r^2(s, \mathbf{x}) = |\mathbf{c}_p(s) - \mathbf{x}|^2 = \sum_{k=0^5} a_k(s - s_{\mathbf{x}})^k \tag{24}$$

with the following coefficients valid in the neighbourhood of some chosen point of expansion, s_0 (with $\kappa_0, \tau_0, \dot{\kappa}_0$ evaluated at s_0)

$$a_0 = r^2 \tag{25}$$
$$a_1 = 0 \tag{26}$$
$$a_2 = 1 - \kappa_0 r\cos\phi \tag{27}$$
$$a_3 = -\frac{r}{3}(\kappa_0\tau_0\sin\phi + \dot{\kappa}_0\cos\phi) \tag{28}$$
$$a_4 = -\frac{\kappa_0^2}{12} \tag{29}$$
$$a_5 = 0 \tag{30}$$
$$a_6 = 0, \tag{31}$$

The third and fourth order terms a_3, a_4 become non-negligeable for very high azimuth resolution modes such as the terrasar-X staring spotlight mode, [6].

[2]at broadside, the tangent vector (aligned with the satellite velocity vector) is perpendicular to the vector connecting the satellite position vector with the target vector

Note that the expression for $\mathbf{x}$ has been defined by the point $s_{\mathbf{x}}$ where the satellite tangent vector makes a right angle to the range vector. The expression can be modified to any other angle if one desires to incorporate a squint angle.

6 The SAR signal in arclength space

This section derives the signal model for a single channel in the wavenumber domain. The term channel refers to a transmit and receive pair and each channel, considered here in isolation, is assumed to be a component of a multi-channel system. The signal derived in this section applies to wideband systems. Special care is taken to ensure that the antenna pattern gain functions are accurately represented as they play an important role in multi-channel signal processing algorithms. The material in this section reviews some concepts already published in the SAR literature, [7–11], but with greater care given to the antenna patterns and with, in some cases, simplified derivations.

As introduced in [12], let the parameterized satellite position is given by $\mathbf{c}(s)$ while the point scatterer position is given by $\mathbf{x}$. In the chosen coordinate system, the point scatterer is not moving, only the satellite.

At the front-end of the sequence of operations, electronic components mix a desired baseband waveform, $p(\tau)$, up to the carrier frequency, ω_0, to yield the signal to be transmitted[3]. This signal is represented as the real part of

$$z(\tau) = p(\tau)e^{i\omega_0\tau} \tag{32}$$

The signal travels down to the surface and a delayed version returns to the radar after reflection from the terrain. For any given s, the distance that the signal must travel is given by

$$2|\mathbf{c}(s) - \mathbf{x}| = 2|\mathbf{r}(s, \mathbf{x})| = 2r(s, \mathbf{x}) \tag{33}$$

If the wave propagates with speed c, then the measured return signal is proportional to

$$z\left(\tau - \frac{2r(s, \mathbf{x})}{c}\right) \tag{34}$$

[3]Waveforms can also be generated directly at the carrier.

6.1 Scene measurement through multiple antenna patterns

The following considers a single element of a multi-aperture antenna system. This single element is composed of a transmit and a receive antenna where the transmit and receive antennas are described by their gain patterns and phase characteristics. As a specific example, such an element could be realized by utilizing subapertures on a phased-array as described in Section E.

Each antenna pattern in the system plays a critical role in multi-channel signal processing. Simple antennas, such as the dipole antenna, and simple antenna models, such as a uniformly-excited aperture or the uniformly-spaced phased-array factor, yield directivity patterns that depend on the wavelength and have beamwidths and gain patterns which depend on the dimensions of the antenna in a given coordinate system.

For an antenna in the far-field, the effective antenna pattern may be represented as

$$\mathrm{A}_n[\hat{\mathbf{r}}(s,\mathbf{x}),\mathbf{p}_n(s)] = e^{-2\frac{2\pi i}{\lambda}\hat{\mathbf{r}}(s,\mathbf{x})\cdot\mathbf{p}_n(s)}\mathrm{D}_n[\lambda,\hat{\mathbf{r}}(s,\mathbf{x})] \tag{35}$$

where λ is the narrowband wavelength, $\mathbf{p}_n(s)$ represents the coordinate of the phase-centre of antenna n in a reference frame centered on the radar platform, $\mathrm{D}_n(\cdot)$ is the two-way antenna pattern amplitude (the product of the transmit antenna pattern and the receive antenna pattern), and $\hat{\mathbf{r}}(s,\mathbf{x})$ is the look vector is defined as $\hat{\mathbf{r}}(s,\mathbf{x}) = \mathbf{r}(s,\mathbf{x})/r(s,\mathbf{x})$. If the two-way antenna pattern depends on two different phase-centres, located at $\mathbf{p}_{n_{\mathrm{Tx}}}(s)$ and $\mathbf{p}_{n_{\mathrm{Rx}}}(s)$, then we define

$$\mathbf{p}_n(s) = \frac{1}{2}[\mathbf{p}_{n_{\mathrm{Tx}}}(s) + \mathbf{p}_{n_{\mathrm{Rx}}}(s)] \tag{36}$$

The wideband generalization sees different values for the carrier wavelength in (35) so that as λ increases, the antenna can measure over a larger range of angles. Conversely, as λ decreases, the antenna beamwidth narrows.

By defining $2\pi/\lambda = (\omega+\omega_0)/c = k_r/2$, one can write the argument to the antenna pattern as

$$\mathrm{A}_n[k_r,\hat{\mathbf{r}}(s,\mathbf{x})] = e^{-ik_r\hat{\mathbf{r}}(s,\mathbf{x})\cdot\mathbf{p}_n(s)}\mathrm{D}_n[k_r,\hat{\mathbf{r}}(s,\mathbf{x})] \tag{37}$$

where, now, k_r is not constant, but free to wander over a range of values to accommodate a wideband model.

We assume from here onwards that the antennas are "steered" so that they maintain a constant orientation relative to the satellite track in a coordinate sytem where the scene is stationary. That is, for regular non moving targets on the Earth's surface, the antennas are fixed relative to the ECEF coordinate track (this is the reason that this paper develops the satellite curve in the ECEF coordinate system). By using the basis vectors developed in the previous section, this means that the antenna patterns can be described as

$$\mathbf{p}_n(s) = \alpha_n \mathbf{T}(s) + \beta_n \mathbf{N}(s) + \gamma_n \mathbf{B}(s), \tag{38}$$

where $\alpha_n, \beta_n, \gamma_n$ are constant with s. It is advantageous to rewrite the above symbolically as

$$\mathbf{p}_n(s) = \alpha_{\|_n} \mathbf{T}(s) + \boldsymbol{\alpha}_{\perp n} \cdot \begin{bmatrix} \mathbf{N}(s) \\ \mathbf{B}(s) \end{bmatrix}, \tag{39}$$

where $\alpha_{\|_n}$ is the projection of $\mathbf{p}_n(s)$ onto the direction of travel, $\mathbf{T}(s)$, while $\boldsymbol{\alpha}_{\perp n}$ is the vector component of $\mathbf{p}_n(s)$ that is perpendicular to $\mathbf{T}(s)$.

Accompanying the phase component of the antenna pattern, the gain can be described as

$$\mathrm{D}_n[k_r, \hat{\mathbf{r}}(s,\mathbf{x})] = \mathrm{D}_n[k_r, \hat{\mathbf{r}}(s,\mathbf{x}) \cdot \mathbf{T}(s), \hat{\mathbf{r}}(s,\mathbf{x}) \cdot \mathbf{N}(s), \hat{\mathbf{r}}(s,\mathbf{x}) \cdot \mathbf{B}(s)] \tag{40}$$

We assume that the gain-pattern model consists of an azimuth component (aligned with the direction of satellite motion) and an elevation component (oriented perpendicular to the direction of motion). This assumption holds for a rectangular array with one dimension of the array aligned along the satellite direction of motion. More specifically, we model the gain-pattern as

$$\begin{aligned} &\mathrm{D}_n[k_r, \hat{\mathbf{r}}(s,\mathbf{x}) \cdot \mathbf{T}(s), \hat{\mathbf{r}}(s,\mathbf{x}) \cdot \mathbf{N}(s), \hat{\mathbf{r}}(s,\mathbf{x}) \cdot \mathbf{B}(s)] \\ &= \mathrm{D}_{\mathrm{az}_n}[k_r, \hat{\mathbf{r}}(s,\mathbf{x}) \cdot \mathbf{T}(s)] \mathrm{D}_{\mathrm{el}_n}[k_r, \hat{\mathbf{r}}(s,\mathbf{x}) \cdot \mathbf{N}(s), \hat{\mathbf{r}}(s,\mathbf{x}) \cdot \mathbf{B}(s)] \end{aligned} \tag{41}$$

The measured return signal consists of the superposition of the reflected signal from various locations over the terrain; thus, for some s, the overall return signal is given by

$$ss_n(\tau, s) = \int \mathrm{A}_n[k_r, \hat{\mathbf{r}}(s,\mathbf{x}), \mathbf{p}_n(s)] \frac{g(\mathbf{x})}{r^2(s,\mathbf{x})} z\left(\tau - \frac{2r(s,\mathbf{x})}{c}\right) \mathrm{d}\mathbf{x} \tag{42}$$

where $g(\mathbf{x}) \in \mathcal{C}$ denotes a random function which represents the scattering response of the point scatterer at $\mathbf{x}$, and the term $r^2(s,\mathbf{x})$ in the denominator

accounts for the fact that in the far-field, electric fields decay at a rate given by the inverse of the range, and the expression accounts for a two-way propagation of an electric field. Without loss of generality, other constant factors from the radar equation have been omitted. In any practical calculation that requires computation of the snr, an account can be made for these factors.

6.2 Demodulation

If the return signal is mixed with $e^{-i\omega_0\tau}$, and if filters are applied to remove unwanted images, one obtains the demodulated signal

$$ss_n(\tau, s) \to ss_n(\tau, s) = \int \mathrm{A}_n[k_r, \hat{\mathbf{r}}(s, \mathbf{x}), \mathbf{p}_n(s)] \frac{g(\mathbf{x})}{r^2(s, \mathbf{x})} p\left(\tau - \frac{2r(s, \mathbf{x})}{c}\right) \cdot e^{-i\omega_0 \frac{2r(s,\mathbf{x})}{c}} \mathrm{d}\mathbf{x} \tag{43}$$

The fast-time FT of $ss_n(\tau, s)$ may be computed as

$$Ss_n(\omega, s) = P(\omega) \int e^{-i\frac{2[\omega+\omega_0]}{c} r(s,\mathbf{x})} \mathrm{A}_n[k_r, \hat{\mathbf{r}}(s, \mathbf{x}), \mathbf{p}_n(s)] \frac{g(\mathbf{x})}{r^2(s, \mathbf{x})} \mathrm{d}\mathbf{x} \tag{44}$$

Recall that $k_r = \frac{2(\omega+\omega_0)}{c}$, and define $k_{r'} = \frac{2\omega}{c}$ and $k_{r_0} = \frac{2\omega_0}{c}$, to yield the processed fast-time frequency signal

$$\mathcal{S}s_n(k_r, s) = \mathcal{P}(k_{r'}) \int e^{-ik_r r(s,\mathbf{x})} \mathrm{A}_n[k_r, \hat{\mathbf{r}}(s, \mathbf{x}), \mathbf{p}_n(s)] \frac{g(\mathbf{x})}{r^2(s, \mathbf{x})} \mathrm{d}\mathbf{x} \tag{45}$$

where $\mathcal{P}(k_{r'}) = |P(ck_{r'}/2)|$ and the absolute value has been computed by multiplying by the known conjugate phase of $P(\cdot)$. Indeed, range or pulse compression is achieved through multiplication by the conjugate phase. For instance, if the pulse is a chirp, then it is at this point that the chirp phase is removed.

6.3 Stationary phase approximation

The Fourier transform over s is given by

$$\begin{aligned}\mathcal{SS}_n(k_r, k_s) &= \int \mathcal{S}s_n(k_r, s) \exp\Big(-ik_s s\Big) \mathrm{d}s \\ &= \mathcal{P}(k_{r'}) \iint \mathrm{A}_n[k_r, \hat{\mathbf{r}}(s, \mathbf{x}), \mathbf{p}_n(s)] \frac{g(\mathbf{x})}{r^2(s, \mathbf{x})} e^{-ik_r r(s,\mathbf{x}) - ik_s s} \mathrm{d}\mathbf{x}\mathrm{d}s.\end{aligned} \tag{46}$$

The stationary phase procedure is an asymptotic approximation procedure that can be used to accurately approximate the above integral. The approximation is given by

$$\int f(s) e^{i\Phi(s)} \mathrm{d}s = e^{i\Phi(s_p)} f(s_p) \sqrt{\frac{2\pi i}{\ddot{\Phi}(s_p)}}, \tag{47}$$

where s_p is the value of s such that $\dot{\Phi}(s_p) = 0$ and $f(s)$ is some slowly varying smooth function. The approximation becomes ever more accurate for increasing values of the second derivative, $\ddot{\Phi}(s_p)$, [13].

We shall apply the above approximation to compute the Fourier transform in (46) by setting

$$f(s) = \mathrm{A}_n[k_r, \hat{\mathbf{r}}(s, \mathbf{x}), \mathbf{p}_n(s)] \frac{g(\mathbf{x})}{r^2(s, \mathbf{x})} \tag{48}$$

and

$$\Phi(s) = -k_r r(s, \mathbf{x}) - k_s s \tag{49}$$

By taking the derivative of $\Phi(s)$ and equating the result to zero, one finds that s_p is the solution to the following equation

$$k_s = -k_r \frac{\mathrm{d}r(s, \mathbf{x})}{\mathrm{d}s} = -k_r \hat{\mathbf{r}}(s, \mathbf{x}) \cdot \frac{\mathrm{d}\{\mathbf{c}(s) - \mathbf{x}\}}{\mathrm{d}s} = -k_r \hat{\mathbf{r}}(s, \mathbf{x}) \cdot \mathbf{T}(s) \tag{50}$$

One notes that the above expression is found in the first part of (39).

7 Stationary phase

This section presents the results of applying the stationary phase approximation to the fast-time, arclength parameterized signal model. The final result

is seen to be a generalization of the classical hyperbolic model with additional terms of the higher order a_3 and a_4 appearing in the range equation and the Stolz interpolation.

We shall find at the end of the section that the presence of the higher order terms results in a Stolz interpolation scheme where there is no closed form for the interpolation points. Instead, interpolation points are given as the roots of a mathematical expression and are assumed (and demonstrated) to be numerically computable.

Recall from (24) that

$$\begin{aligned} r(s,\mathbf{x}) &= \sqrt{|\mathbf{c}_p(s)-\mathbf{x}|^2} = \sqrt{\sum_{k=0^4} a_k (s-s_{\mathbf{x}})^k} \\ &= \sqrt{r^2 + a_2(s-s_{\mathbf{x}})^2 + a_3(s-s_{\mathbf{x}})^3 + a_4(s-s_{\mathbf{x}})^4} \end{aligned} \tag{51}$$

The phase of the function in (46) is then given by

$$\Phi(s) = -k_r \sqrt{r^2 + a_2(s-s_{\mathbf{x}})^2 + a_3(s-s_{\mathbf{x}})^3 + a_4(s-s_{\mathbf{x}})^4} - k_s s \tag{52}$$

In order to simplify the calculation, let

$$\begin{aligned} -r\tan\theta_s(s) &= \sqrt{a_2 s^2 + a_3 s^3 + a_4 s^4} \\ &= s\sqrt{a_2 + a_3 s + a_4 s^2} \\ &= s g(s) \end{aligned} \tag{53}$$

The above relation is really only a mathematical convenience; however, in the simple linear trajectory case (i.e..airborne SAR), the angle $\theta_s(s)$ corresponds to the look angle. By substituting this relation in (52), one finds that

$$\begin{aligned} \Phi(s) &= -rk_r \sec\theta_s(s-s_{\mathbf{x}}) - k_s s \\ &= -rk_r \sec\theta_s(s-s_{\mathbf{x}}) - k_s(s-s_{\mathbf{x}}) - k_s s_{\mathbf{x}} \end{aligned} \tag{54}$$

Now

$$\begin{aligned} \frac{\mathrm{d}\Phi(s)}{\mathrm{d}s} &= \frac{\mathrm{d}\Phi(s)}{\mathrm{d}(s-s_{\mathbf{x}})}\frac{\mathrm{d}(s-s_{\mathbf{x}})}{\mathrm{d}s} \\ &= -rk_r \tan\theta_s(s-s_{\mathbf{x}})\sec\theta_s(s-s_{\mathbf{x}})\frac{\mathrm{d}\theta_s(s-s_{\mathbf{x}})}{\mathrm{d}(s-s_{\mathbf{x}})} - k_s, \end{aligned} \tag{55}$$

and the stationary phase prescription instructs that this should be equated to zero, thus

$$-rk_r \tan\theta_s(s-s_{\mathbf{x}}) \sec\theta_s(s-s_{\mathbf{x}}) \frac{\mathrm{d}\theta_s(s-s_{\mathbf{x}})}{\mathrm{d}(s-s_{\mathbf{x}})} = k_s. \tag{56}$$

On the other hand, by taking the derivative of (53), one calculates that

$$-r\sec^2\theta_s(s-s_{\mathbf{x}}) \frac{\mathrm{d}\theta_s(s-s_{\mathbf{x}})}{\mathrm{d}(s-s_{\mathbf{x}})} = g(s-s_{\mathbf{x}}) + (s-s_{\mathbf{x}}) \frac{\mathrm{d}g(s-s_{\mathbf{x}})}{\mathrm{d}(s-s_{\mathbf{x}})}, \tag{57}$$

which means that the stationary phase value s_p is the value which satisfies

$$k_r \sin\theta_s(s_p-s_{\mathbf{x}}) \left[g(s_p-s_{\mathbf{x}}) + (s_p-s_{\mathbf{x}}) \frac{\mathrm{d}g(s_p-s_{\mathbf{x}})}{\mathrm{d}(s_p-s_{\mathbf{x}})} \right] = k_s. \tag{58}$$

By letting $s^* = s_p - s_{\mathbf{x}}$, the preceding becomes

$$k_r \sin\theta_s(s^*) \left[g(s^*) + s^* \frac{\mathrm{d}g(s^*)}{\mathrm{d}s^*} \right] = k_s. \tag{59}$$

7.1 Relation between arclength and wavenumber

The remainder of this section seeks to present a means to invert (59), that is, to compute some form of s_p or θ_s given wavenumbers k_s and k_r.

This subsection develops one of the key approximations used to derive the Stolz interpolation points. We begin by recalling from (53) that

$$-r\tan\theta_s(s) = sg(s) \tag{60}$$

Let us write this as

$$y = sg(s) \tag{61}$$

To invert the above, we note that

$$\begin{aligned} s &= \frac{y}{g(s)} = \frac{y}{g\left(\frac{y}{g(s)}\right)} \\ &\approx \frac{y}{g\left(\frac{y}{g(0)}\right)} \end{aligned} \tag{62}$$

which also leads to the approximation that

$$g(s) \approx g\left(\frac{y}{g(0)}\right) \tag{63}$$

The above two equations are the key expressions used in the approximation. Note that, by once again substituting the expression for s into the right side of (62), this subsection could have developed the approximation to potentially even greater accuracy[4]. For the purposes of this work, the approximation as written in (62) appears to be more than adequate.

From the definition of $g(s)$, one computes that

$$g(s) + s\frac{\mathrm{d}g(s)}{\mathrm{d}s} = g(s) + \frac{a_3 s + 2a_4 s^2}{2g(s)}. \tag{64}$$

Thus,

$$\begin{aligned} g(s) + s\frac{\mathrm{d}g(s)}{\mathrm{d}s} &\approx g\left(\frac{y}{g(0)}\right) + \frac{a_3 y}{2g^2\left(\frac{y}{g(0)}\right)} + \frac{a_4 y^2}{g^3\left(\frac{y}{g(0)}\right)} \\ &= g\left(\frac{-r\tan\theta_s(s)}{\sqrt{a}_2}\right) - \frac{a_3 r\tan\theta_s(s)}{2g^2\left(\frac{-r\tan\theta_s(s)}{\sqrt{a}_2}\right)} + \frac{a_4 r^2\tan^2\theta_s(s)}{g^3\left(\frac{-r\tan\theta_s(s)}{\sqrt{a}_2}\right)} \end{aligned} \tag{65}$$

The above can be inserted into (59) to yield an expression that relates, on the left, a function that depends on $\sin\theta_s(s^*)$ (which is written as $\sin\theta_s$, with $\tan\theta_s = \sin\theta_s/\sqrt{1-\sin^2\theta_s}$) to, on the right, a function of k_r, k_s.

$$\sin\theta_s\left[g\left(\frac{-r\tan\theta_s}{\sqrt{a}_2}\right) - \frac{a_3 r\tan\theta_s}{2g^2\left(\frac{-r\tan\theta_s}{\sqrt{a}_2}\right)} + \frac{a_4 r^2\tan^2\theta_s}{g^3\left(\frac{-r\tan\theta_s}{\sqrt{a}_2}\right)}\right] = \frac{k_s}{k_r}. \tag{66}$$

To be specific, the above can be written as

$$f(\sin\theta_s; r) = \frac{k_s}{k_r} \tag{67}$$

and one observes that only in the case that $a_3 = a_4 = 0$ is the above independent of r.

[4]Subject to a mathematical proof that the approximation would improve

One can write (62) as

$$s^* \approx \frac{-r \tan\theta_s}{g\left(\frac{-r\tan\theta_s}{\sqrt{a}_2}\right)} \tag{68}$$

The above allows the phase expression at the stationary point to be written as

$$\begin{aligned}
\Phi(s) &= -rk_r \sec\theta_s (s - s_{\mathbf{x}}) - k_s(s - s_{\mathbf{x}}) - k_s s_{\mathbf{x}} \\
&= -rk_r \sec\theta_s + rk_s \frac{\tan\theta_s}{g\left(\frac{-r\tan\theta_s}{\sqrt{a}_2}\right)} - k_s s_{\mathbf{x}} \\
&= -r\left[k_r \sec\theta_s - k_s \frac{\tan\theta_s}{g\left(\frac{-r\tan\theta_s}{\sqrt{a}_2}\right)}\right] - k_s s_{\mathbf{x}}.
\end{aligned} \tag{69}$$

By inverting (67), one can compute $\sin\theta_s$ as a function of k_r, k_s. This can be substituted into the above to yield a phase function dependent only upon the spatial wavenumbers (and the range). The first term (the term multiplied by r) in the last line of (69) thus represents a modified Stolz interpolation function which can easily be computed numerically. Appendix D outlines the particular implementation of the numerical approach adopted in this work.

Note that in the case $a_3 = a_4 = 0$, the above reduces to

$$\Phi(s) = -r\sqrt{k_r^2 - \frac{k_s^2}{a_2}} - k_s s_{\mathbf{x}}. \tag{70}$$

7.2 Antenna pattern angles

In this section, we examine the implications of the stationary phase approximatino on the antenna pattern. While the Stolz interpolation and the range equation are critical for single-channel SAR signal processing, multi-channel signal processing further demands an accurate description of the antenna pattern, in this case, in the wavenumber domain. The material presented in this section relies heavily upon both the Frenet-eret equations and the vector calculus expansions referenced in Appendix A.

Before switching to the main content of this section, it is worth discussing some of the physical implications of the results presented at the end.

One of the primary results shows that in the neighbourhood of some ground point, chosen for SAR processing, the multi-channel singal reconstruction algorithms can be considered independent of the range wavenumber, k_r[5]. Signals from the multiple channels can be combined into a single response, equivalent to what one would have expected from a single adequately-sampled SAR, without regard to a varying k_r. This simplifies the multi-channel signal processing. Note that after multi-channel signal processing, the produced signal still needs to be SAR processed, and this SAR processing does depend on k_r.

Assume that the point around which we wish to SAR process the signals is given by r_0, s_{t_0}, ϕ_0. Our objective is to expand the signals around this point with the demonstrated assumption that over a neighbourhood of significant size, the expansion is accurate enough for SAR processing.

The quantities $\hat{\mathbf{r}}(s,\mathbf{x})\cdot\mathbf{T}(s)$, $\hat{\mathbf{r}}(s,\mathbf{x})\cdot\mathbf{N}(s)$ and $\hat{\mathbf{r}}(s,\mathbf{x})\cdot\mathbf{B}(s)$ all appear in the antenna pattern arguments, both in the phase component through

$$e^{-ik_r\hat{\mathbf{r}}(s,\mathbf{x})\cdot\mathbf{p}_n(s)} \tag{71}$$

since

$$\hat{\mathbf{r}}(s,\mathbf{x})\cdot\mathbf{p}_n(s) = \alpha_{\parallel_n}\hat{\mathbf{r}}(s,\mathbf{x})\cdot\mathbf{T}(s) + \boldsymbol{\alpha}_{\perp n}\cdot\begin{bmatrix}\hat{\mathbf{r}}(s,\mathbf{x})\cdot\mathbf{N}(s)\\ \hat{\mathbf{r}}(s,\mathbf{x})\cdot\mathbf{B}(s)\end{bmatrix}, \tag{72}$$

and in the antenna gain component through

$$\begin{aligned}&\mathrm{D}_n[k_r,\hat{\mathbf{r}}(s,\mathbf{x})] =\\ &\quad \mathrm{D}_{\mathrm{az}_n}[k_r,\hat{\mathbf{r}}(s,\mathbf{x})\cdot\mathbf{T}(s)]\ \mathrm{D}_{\mathrm{el}_n}[k_r,\hat{\mathbf{r}}(s,\mathbf{x})\cdot\mathbf{N}(s),\hat{\mathbf{r}}(s,\mathbf{x})\cdot\mathbf{B}(s)].\end{aligned} \tag{73}$$

According to (47), these all need to evaluated at the stationary point s_p. We have already seen from equation (50) that

$$\hat{\mathbf{r}}(s_p)\cdot\mathbf{T}(s_p) = -k_s/k_r \tag{74}$$

Appendix F further calculates that

$$\hat{\mathbf{r}}(s_p)\cdot\mathbf{N}(s_p) \approx \cos\phi_0 + \frac{r}{r_0}\sin\phi_0\sin(\phi-\phi_0) \tag{75}$$

$$\hat{\mathbf{r}}(s_p)\cdot\mathbf{B}(s_p) \approx \sin\phi_0 - \frac{r}{r_0}\cos\phi_0\sin(\phi-\phi_0) \tag{76}$$

[5]This independence does not include potential implementation of a frequency domain implementation of a fast-time delay

Which leads the following

$$\begin{aligned}&\alpha_{\parallel_n} k_r \hat{\mathbf{r}}(s_p) \cdot \mathbf{T}(s_p) + k_r \boldsymbol{\alpha}_{\perp n} \cdot \begin{bmatrix} \hat{\mathbf{r}}(s_p) \cdot \mathbf{N}(s_p) \\ \hat{\mathbf{r}}(s_p) \cdot \mathbf{B}(s_p) \end{bmatrix} \\ &= -\alpha_{\parallel_n} k_s + k_r \boldsymbol{\alpha}_{\perp n} \cdot \hat{\mathbf{r}}_0 + k_r r \frac{\boldsymbol{\alpha}_{\perp n} \cdot \hat{\mathbf{r}}_{0\perp}}{r_0} \sin(\phi - \phi_0)\end{aligned} \tag{77}$$

The above shows that even in the case of an across-track baseline, it is the component of this baseline in the look direction (the second term, $k_r \boldsymbol{\alpha}_{\perp n} \cdot \hat{\mathbf{r}}_0$) that has most effect on the multi-channel phase. This physically makes sense as the ranges to the targets on the ground do not change significantly with across-track baselines in the cross-look-direction. The expression further shows that a compenstation for the look-direction component of the across-track baseline can be computed and applied in the neighbourhood of the selected expansion point. This correction should be applied before any azimuth processing so as to eliminate the majority of effects stemming from an across-track baseline.

Assuming that the across-track compensation has been applied, i.e. that the signal has been multiplied by

$$H_{al} = e^{ik_r \boldsymbol{\alpha}_{\perp n} \cdot \hat{\mathbf{r}}_0}, \tag{78}$$

and that the component in the cross-look direction,

$$H_{cl} = e^{-ik_r r \frac{\boldsymbol{\alpha}_{\perp n} \cdot \hat{\mathbf{r}}_{0\perp}}{r_0} \sin(\phi - \phi_0)} \to 1, \tag{79}$$

the expression for the signal in k-space is given by

$$\mathcal{SS}_n(k_r, k_s) = e^{i\alpha_{\parallel_n} k_s} \mathrm{D}_{\mathrm{az}_n}[k_r, -k_s/k_r] \Phi_n(k_r, k_s) \tag{80}$$

where

$$\Phi_n(k_r, k_s) = \mathcal{P}(k_{r'}) \int \frac{g(\mathbf{x}) \mathrm{D}_{\mathrm{el}_n}[k_r, \cos\phi, \sin\phi]}{r^2(s_p[k_r, k_s])} e^{-ik_r r(s_p[k_r, k_s])} \mathrm{d}\mathbf{x} \tag{81}$$

In the case that the elevation component of the gain pattern is constant across all channels, the above simplifies to

$$\mathcal{SS}_n(k_r, k_s) = e^{i\alpha_{\|_n} k_s} \mathrm{D}_{\mathrm{az}_n}[k_r, -k_s/k_r] \Phi(k_r, k_s) \tag{82}$$

where

$$\Phi(k_r, k_s) = \mathcal{P}(k_{r'}) \int \frac{g(\mathbf{x}) \mathrm{D}_{\mathrm{el}}[k_r, \cos\phi, \sin\phi]}{r^2(s_p[k_r, k_s])} e^{-ik_r r(s_p[k_r, k_s])} \mathrm{d}\mathbf{x} \tag{83}$$

8 Multi-channel SAR processing

With the signal represented in the 2-D frequency domain we are finally ready to derive the multi-channel processing filters.

This section derives signal processing methods to reconstruct an optimal scalar spectrum for wideband SAR imaging. It is assumed that the antennas are fixed relative to track - *i.e.*, that one can model the signal according to (80). Further, it is assumed that the antenna positions relative to track are known. The relative motion parameters are also known and the objective is to reproduce a high-resolution image from the multi-channel signal which is aliased according to the PRF.

8.1 Linear filtering to extract signal components

The linear filtering approach applies a multi-dimensional filter in the wavenumber domain so that a scalar reconstructed signal, denoted by $\mathcal{ZZ}_R(k_r, k_s)$, is created via

$$\mathcal{ZZ}_R(k_r, k_s + lk_{s_p}) = \mathbf{b}_l^\dagger(k_r, k_s) \mathbf{z}(k_r, k_s) \tag{84}$$

The challenge is to find the vectors $\mathbf{b}_l(k_r, k_s)$ that yield the desired quality of signal. The goal of this section is to determine appropriate choices for $\mathbf{b}_l(k_r, k_s)$ such that the reconstructed, scalar signal,

$$\mathcal{ZZ}_R(k_r, k_s + lk_{s_p}) = \mathbf{b}_l^\dagger(k_r, k_s) \mathbf{z}(k_r, k_s) \tag{85}$$

is as free from azimuth ambiguities as possible and that it does not suffer catastrophic losses in snr.

8.2 Matrix-vector model for the aliased signal

The derivation of the filters is aided by rewriting the multi-channel signal in matrix-vector notation.

Recall that an N-channel system measurement can be represented as

$$\begin{aligned}\mathbf{z}(k_r, k_s) &= \sum_{l\in\mathcal{L}} \mathbf{s}(k_r, k_s + lk_{s_p}) + \mathbf{n}(k_r, k_s) \\ &= \sum_{l\in\mathcal{L}} \mathbf{a}(k_r, k_s)\Phi(k_r, k_s + lk_{s_p}) + \mathbf{n}(k_r, k_s)\end{aligned} \tag{86}$$

where

$$\mathbf{a}(k_r, k_s) = \begin{bmatrix} e^{i\alpha_{\parallel 1}k_s}\mathrm{D}_{\mathrm{az}_1}[k_r, -k_s/k_r] \\ e^{i\alpha_{\parallel 2}k_s}\mathrm{D}_{\mathrm{az}_2}[k_r, -k_s/k_r] \\ \cdots \\ e^{i\alpha_{\parallel N}k_s}\mathrm{D}_{\mathrm{az}_N}[k_r, -k_s/k_r] \end{bmatrix} \tag{87}$$

and $\Phi(k_r, k_s)$ is defined in (83).

The summation can be incorporated into a matrix multiplication to yield

$$\begin{aligned}\mathbf{z}(k_r, k_s) &= \mathbf{H}(k_r, k_s)\boldsymbol{\Phi}(k_r, k_s) \\ &\quad + \mathbf{n}(k_r, k_s)\end{aligned} \tag{88}$$

where the matrix $\mathbf{H}$ is composed of the vectors $\mathbf{a}$ according to

$$\mathbf{H}(k_r, k_s) = \begin{bmatrix}\ldots & \mathbf{a}(k_r, k_s - k_{s_p}) & \mathbf{a}(k_r, k_s) & \ldots\end{bmatrix} \tag{89}$$

and

$$\boldsymbol{\Phi}(k_r, k_s) = \begin{bmatrix} \vdots \\ \Phi(k_r, k_s - k_{s_p}) \\ \Phi(k_r, k_s) \\ \vdots \end{bmatrix} \tag{90}$$

The matrix $\mathbf{H}$ may be fat, skinny or square[6] according to the number of channels and the degree of aliasing of a band-limited signal.

[6] A matrix of size $m \times n$ is square if $m = n$, skinny if $m > n$, and fat if $m < n$.

8.3 A cost function for HRWS processing

Our wish is to multiply the measured signal in (88) by some matrix, $\mathbf{B}(k_r, k_s)$, such that $\mathbf{B}(k_r, k_s)\mathbf{H}(k_r, k_s) = \mathbf{D}(k_r, k_s)$ where $\mathbf{D}(k_r, k_s)$ is some desired diagonal matrix. This desired matrix, resulting from the product, should ideally be one that provides good radiometric resolution. A practical choice is, for instance, the average antenna pattern. Note that if $\mathbf{D}(k_r, k_s)$ is diagonal, then it is straight-forward to read the individual aliased components of the signal as they will just correspond to the diagonal element of $\mathbf{D}(k_r, k_s)$ multiplied by the corresponding row of $\boldsymbol{\Phi}(k_r, k_s)$.

In particular, because, heuristically, we are interested in the signal measured by the *average* antenna pattern, let the diagonal elements of $\mathbf{D}(k_r, k_s)$ be given by

$$D_{ll}(k_r, k_s) = \sqrt{\sum_n |\mathrm{D}_{\mathrm{az}_n}[\hat{\mathbf{r}}_l(k_r, k_s)]|^2} \tag{91}$$

where

$$\hat{\mathbf{r}}_l(k_r, k_s) = \hat{\mathbf{r}}(k_r, k_s + lk_{s_p}) \tag{92}$$

For different values of l, the range look vector points in different directions. Our choice of $\mathbf{D}(k_r, k_s)$ contains elements corresponding to the signal returned from the different directions corresponding to l (weighted by the average antenna pattern). This provides a mechanism to extract the unambiguous signal.

The minimum square error approach to computing $\mathbf{B}(k_r, k_s)$ seeks to minimise the following cost function

$$J_0 = |\mathbf{B}(k_r, k_s)\mathbf{H}(k_r, k_s) - \mathbf{D}(k_r, k_s)|^2 \tag{93}$$

where $|\cdot|^2$ denotes the Frobenius norm.

8.3.1 Amplified additive noise

Before attempting to find minimum values for J_0, one should recognise that if we pre-multiply $\mathbf{z}(k_r, k_s)$ by $\mathbf{B}(k_r, k_s)$, then the additive noise term is also pre-multiplied by $\mathbf{B}(k_r, k_s)$ and this might adversely change the snr. Thus, one should simultaneously try to minimise the following cost function

$$J_1 = \mathcal{E}\{|\mathbf{B}(k_r, k_s)\boldsymbol{\nu}(k_r, k_s)|^2\} \tag{94}$$

8.3.2 Blended cost function

In the event that the solution to minimising each cost-function is different, a fair trade would see the construction of a tuneable hybrid cost-function given by

$$J_2 = \varrho J_0 + (1-\varrho)J_1 \tag{95}$$

where $\varrho \in (0,1]$. The solution to this problem is computed in [4] yielding the mmse filters given by

$$\mathbf{B}(k_r,k_s) = \mathbf{D}(k_r,k_s)\mathbf{H}^\dagger(k_r,k_s) \left[\mathbf{H}(k_r,k_s)\mathbf{H}^\dagger(k_r,k_s) + \frac{1-\varrho}{\varrho}\mathbf{R}_n(k_r,k_s)\right]^{-1} \tag{96}$$

8.4 Section summary

This section developed the hrws signal processing methods to construct a scalar signal with reduced or eliminated azimuth ambiguities and acceptable snr from a vector of aliased signals. The section derived set of filters that depends on a variable parameter ϱ which controls the level of azimuth ambiguity (or residual aliasing) and the snr. The choice of $\varrho = 1$ leads to the projection filters of [14–16]. In the general wideband case, the hrws processing filters are k_r and k_s dependant, but for systems with no across-track baseline or narrowband systems, the processing filters depend only on k_s.

9 Slow-time curve parameters, state vectors and the geoid model

Section 4.1 produced expressions that depend upon $\mathbf{c}_t(t)$, $\dot{\mathbf{c}}_t(t)$, $\ddot{\mathbf{c}}_t(t)$ and $\dddot{\mathbf{c}}_t(t)$. This section demonstrates how these quantities can be computed from state vectors and the NASA published geoid model (EGM96 or EGM2008).

9.1 State vectors

State vectors provided by vendors often reference the ECEF coordinate system; that is, they are given in an Earth-Centred, Earth Fixed (ECEF) coor-

dinate system. We define the position component of the state vector as $\mathbf{c}_t(t)$ while the velocity component provides $\dot{\mathbf{c}}_t(t)$.

9.2 Geopotential model

Calculation of $\ddot{\mathbf{c}}_t(t)$ and $\dddot{\mathbf{c}}_t(t)$ requires application of a geoid model as the acceleration at any given point depends primarily on the mass distribution of the earth. Secondary factors including drag, lunar and solar gravitation effects and tidal effects are not considered here. It is felt that these effects do not significantly perturb the satellite trajectory over the time periods of even the highest resolution synthetic apertures.

The NIMA/NGA provided geopotential model provides a set of parameters to be used in a spherical harmonic expansion that approximates the earth gravitational potential, https://earth-info.nga.mil/GandG/wgs84/gravitymod/index.html. The prescription yields the graviational potential as a function of radius, latitude, longitude, respectively, $U(r, \phi_s, \lambda_s)$.

$$U(r, \phi_s, \lambda_s) = \frac{GM}{r}\left(1 + \sum_{n=2}^{n_{\max}} \left(\frac{a}{r}\right)^n \sum_{m=0}^{n} \bar{P}_{nm}(\sin\phi_s)\left[\bar{C}_{nm}\cos m\lambda_s + \bar{S}_{nm}\sin m\lambda_s\right]\right) \tag{97}$$

where a is the major axis of the Earth (m), $\bar{P}_{nm}(\cdot)$ are the fully normalized associated Legendre polynomials of degree n and order m, $\bar{C}_{nm}$ and $\bar{S}_{nm}$ are the model coefficients (e.g. egm96, egm2008 from NIMA/NGA). Note that ϕ_s, λ_s are given in a spherical polar coordinates not the common ellipsoidal latitude and longitude as in geography.

The gravitational potential and its derivates, given in spherical polar coordinates, are transformed into Cartesian coordinates in order to calculate the acceleration and rate of change of acceleration. Appendix B.2 outlines how this can be accomplished. A clearly written explanation on how to apply the spehircal harmonics to calculation of satellite trajectories can be found in [17]. This document calculates the satellite acceleration in the ECEF coordinate system; further, the material in Appendix B.2 also considers the rate of change of acceleration as this becomes important in the derivation of the satellite motion over long synthetic apertures.

Note that the gravitational potential is given in an inertial coordinate system. Thus, calculated accelerations must be transformed into an ECEF

coordinate system. Appendix B and [17] show how this transformation can be accomplished.

Figure 5 demonstrates the accuracy of the physical geoid model using precision state vector data obtained from https://qc.sentinel1.eo.esa.int/aux_poeorb/. The plot has been generated by taking a single state vector at slow-time value zero (arbitrarily chosen to be 2018-08-05 16:08:22) and numerically integrating the position of the satellite forty seconds forwards and backwards in time. This numerical result has been computed by using the scipy *integrate.solve_ivp* method in Python3 to integrate the differential equation listed in [17]; in this case with the egm96 geoid model, but without any lunar solar or drag effects. Either side of slow-time zero, the recoded precise state vectors are compared with the numerically integrated result. One sees that, over the course of eighty seconds, the satellite position is within 5 millimeters of the reference position.

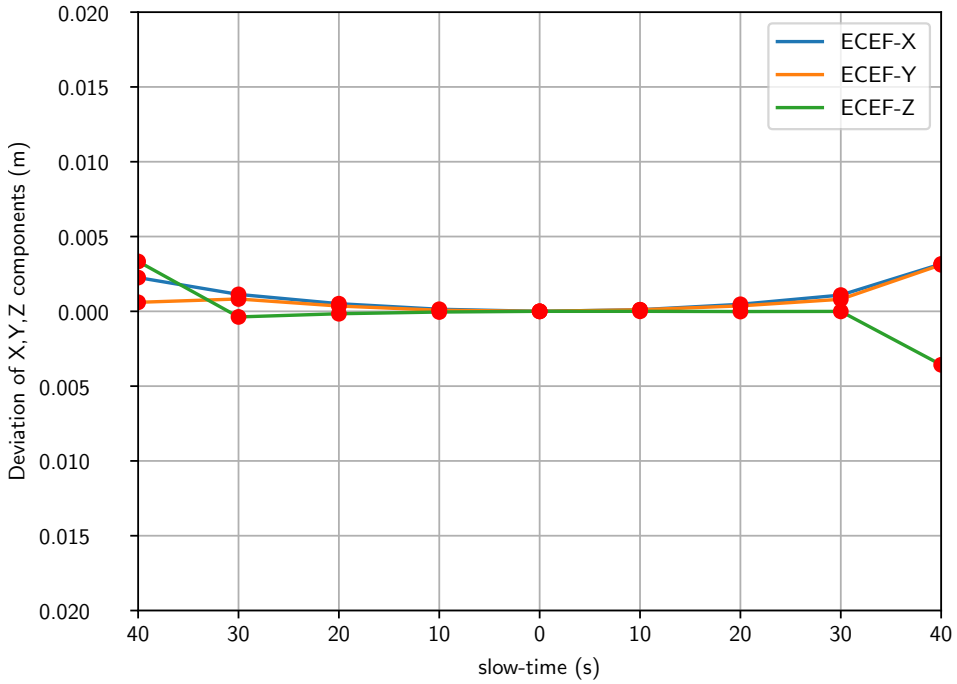

Figure 5: Comparison of numerical integrtaion of the differential equation of satellite motion with recorded precise state vectors sourced from https://qc.sentinel1.eo.esa.int/aux_poeorb/

10 Simulated mutli-channel signal

To demonstrate the signal processing approach, this section generates a simulated signal using the design parameters of a 15cm system. As mentioned, as the resolution decreases (i.e. improves) data capture and storage requirements rapidly increase which also means that hardware requirements for signal processing also increase. The chosen resolution of 15cm, demonstrated in this section, required the use of a machine with approximately 600 gigabytes of RAM, 96 processing cores and was further accelerated using NVIDIA GPU processing. The hardware requirements to simulate a 10cm resolution mode were not available to the authors at the time of writing. In principle, given suitable processing power, such a 10cm mode could be simulated with the same Python-based code.

The simulation, with parameters listed in Table 2, was computed using the numba, numpy, and scipy libraries of Python, with plots generated using Matplotlib. The simulator computes the back-folded signal for each of the

Table 2: Simulation parameters

f_p	5555.56 Hz
L_M	2.7 m
L	24.3 m
$M+1$	9
λ	0.031067 m

81 channels of data, computes the processing filters, applies the filters to the back-folded data and presents the amplitude of the reconstructed signal in the Doppler domain in Figure 6. The response in the Doppler domain shows the desired response in the k_s domain with each local maximum in this region highlighting the response of each sub-beam. The simulator then azimuth compresses this reconstructed signal with a computed chirp and transforms the data back into the spatial domain to produce the Point Spread Function (PSF) shown in Figure 7. This figure illustrates that the system achieves the desired resolution with the response width less than 0.1 m at the -5 dB level. While the figure also shows a second set of sidelobes at -15 dB, it is assumed that these can be reduced by an appropriate choice of weighting on the antenna patterns.

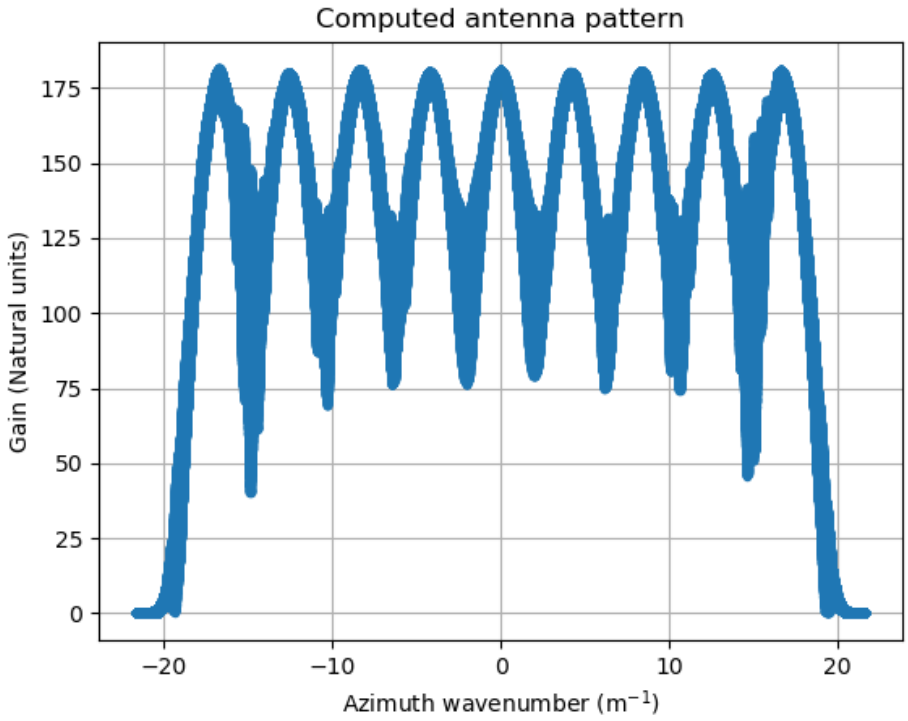

Figure 6: Response of the reconstructed signal in the Doppler domain.

A test noise signal is also generated by the simulator. The SNR prior to filtering is compared with the SNR after filtering (but before azimuth compression) giving a change of about -0.4 dB. This shows that with the simulated parameters, the SNR does not change significantly.

In summary, the simulation demonstrates the suitability of the proposed signal processing algorithm and also shows how the generated PSF contains extra sidelobes that most likely result from the different shape of the signal response in the Doppler domain. If these sidelobes are intolerable, they can possibly be removed by modifying the phased-array beam tables; however, this is a topic for further research.

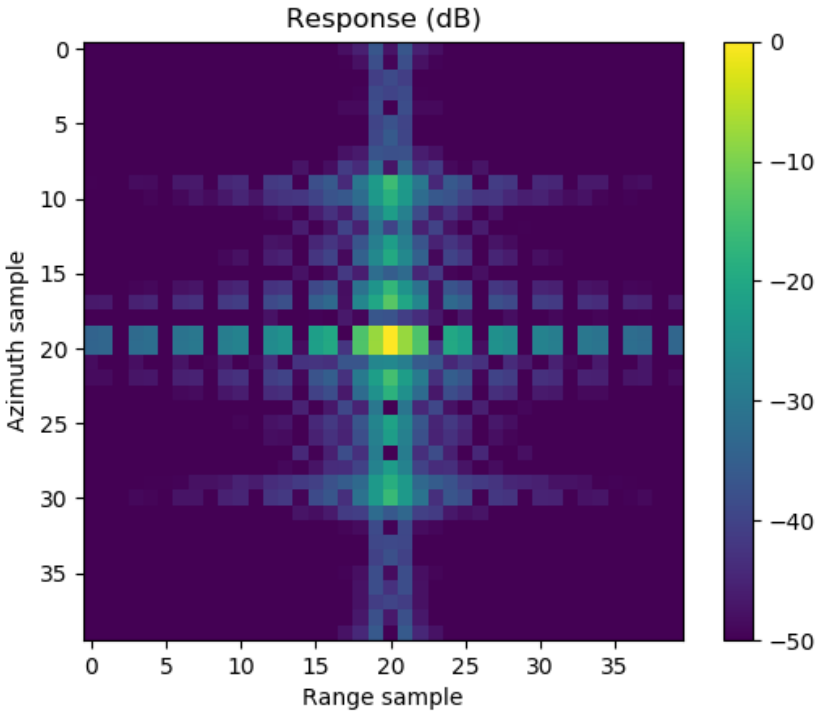

Figure 7: Point Spread Function using the described processing method.

11 Conclusion

This letter proposes a system for improved space-based SAR imaging, describing the design, which is based upon a phased-array and an appropriate switching network to allow digitisation of multiple receive channels, the configuration, which imposes a rapid electronic beam switching capability upon the design, and a suitable signal processing algorithm to compute the high resolution imagery. The proposed configuration permits measurement of a relatively large swath in a Stripmap-like mode, thereby offering, theoretically, unlimited azimuth extent. On the other hand, as demonstrated by the test example of 10cm azimuth resolution considered throughout the paper, the resolution of the imagery can be even better than the highest resolution spotlight imagery available from current commercial systems.

Importantly, the state of current technology is sufficiently advanced to construct such a SAR system.

As a final important consideration, we note that the design does not preclude the use of other traditional measurement modes such as Spotlight, TOPS or ScanSAR. Further, it provides the flexibility to implement other advanced modes such as HRWS and Ground Moving Target Indication.

References

[1] P. Prats-Iraola et al. "On the Processing of Very High Resolution Spaceborne SAR Data". In: *IEEE Transactions on Geoscience and Remote Sensing* 52.10 (Oct. 2014), pp. 6003–6016. ISSN: 0196-2892. DOI: 10.1109/TGRS.2013.2294353.

[2] D. Meng et al. "On the Processing of Very High Resolution Spaceborne SAR Data: A Chirp-Modulated Back Projection Approach". In: *IEEE Transactions on Geoscience and Remote Sensing* 56.1 (Jan. 2018), pp. 191–201. ISSN: 0196-2892. DOI: 10.1109/TGRS.2017.2744649.

[3] Y. Wu et al. "Processing of Very High Resolution Spaceborne Sliding Spotlight SAR Data Using Velocity Scaling". In: *IEEE Transactions on Geoscience and Remote Sensing* 54.3 (Mar. 2016), pp. 1505–1518. ISSN: 0196-2892. DOI: 10.1109/TGRS.2015.2481923.

[4] I. C. Sikaneta and D. Cerutti-Maori. "Novel Radar Techniques and Applications". In: ed. by R. Klemm et al. Raleigh: SciTech Publishing, 2017. Chap. High-resolution wide-swath SAR.

[5] I. Sikaneta, C.H. Gierull, and D. Cerutti-Maori. "Optimum Signal Processing for Multichannel SAR: With Application to High-Resolution Wide-Swath Imaging". In: *Geoscience and Remote Sensing, IEEE Transactions on* 52.10 (Oct. 2014), pp. 6095–6109. ISSN: 0196-2892. DOI: 10.1109/TGRS.2013.2294940.

[6] J. Mittermayer et al. "The TerraSAR-X Staring Spotlight Mode Concept". In: *IEEE Transactions on Geoscience and Remote Sensing* 52.6 (June 2014), pp. 3695–3706. ISSN: 0196-2892. DOI: 10.1109/TGRS.2013.2274821.

[7] I.G. Cumming, Y.L. Neo, and F.H. Wong. "Interpretations of the omega-K algorithm and comparisons with other algorithms". In: *Geoscience and Remote Sensing Symposium, 2003. IGARSS '03. Proceedings. 2003 IEEE International*. Vol. 3. Toulouse, France, July 2003, pp. 1455–1458.

[8] I. G. Cumming and F. H. Wong. *Digital Processing of Synthetic Aperture Radar Data: Algorithms and Implementation*. Norwood, MA: Artech House Remote Sensing Library, 2005. ISBN: 1-58053-058-3.

[9] G. Franceschetti and R. Lanari. *Synthetic Aperture Radar Processing*. Washington: CRC Press, 1999.

[10] R. K. Raney. "A New And Fundamental Fourier Transform Pair". In: *Geoscience and Remote Sensing Symposium, 1992. IGARSS '92. International*. Vol. 1. Houston, TX, USA, May 1992, pp. 106–107. DOI: 10.1109/IGARSS.1992.576640.

[11] R. Bamler. "A comparison of range-Doppler and wavenumber domain SAR focusing algorithms". In: *Geoscience and Remote Sensing, IEEE Transactions on* 30.4 (July 1992), pp. 706–713. DOI: 10.1109/36.158864.

[12] J. H G Ender. "Signal theoretical aspects of bistatic SAR". In: *Geoscience and Remote Sensing Symposium, 2003. IGARSS '03. Proceedings. 2003 IEEE International*. Vol. 3. Toulouse, France, July 2003, pp. 1438–1441. DOI: 10.1109/IGARSS.2003.1294137.

[13] M. R. Spiegel. *Theory and Problems of Complex Variables*. New York: Schaums, 1964.

[14] G. Krieger, N. Gebert, and A. Moreira. "Unambiguous SAR signal reconstruction from nonuniform displaced phase center sampling". In: *Geoscience and Remote Sensing Letters, IEEE* 1.4 (Oct. 2004), pp. 260–264. ISSN: 1545-598X. DOI: 10.1109/LGRS.2004.832700.

[15] N. Gebert and G. Krieger. "Azimuth Phase Center Adaptation on Transmit for High-Resolution Wide-Swath SAR Imaging". In: *Geoscience and Remote Sensing Letters, IEEE* 6.4 (Oct. 2009), pp. 782–786. ISSN: 1545-598X. DOI: 10.1109/LGRS.2009.2025245.

[16] N. Gebert. "Multi-Channel Azimuth Processing for High-Resolution Wide-Swath SAR Imaging". PhD thesis. University of Karlsruhe, 2009.

[17] Ho-Nien Shou. "Orbit Propagation and Determination of Low Earth Orbit Satellites". In: *International Journal of Antennas and Propagation* (2014). URL: https://doi.org/10.1155/2014/903026.

A Derivative of unit vectors

This section provides a summary of well-known vector derivative relations. These relations can be used to tie together many of the mathematical derivations scattered throughout the document.

Specifically, the section presents the derivatives of three forms of a parameterized vector with respect to the parameter. These forms include the derivative of the amplitude of the parameterized vector, the derivative of the parameterized unit vector and the derivative of the projection of a given parameterized vector in the direction perpendicular to another vector with the same parameterization.

Consider

$$\frac{\mathrm{d}|\mathbf{f}|}{\mathrm{d}t} = \hat{\mathbf{f}}^T\dot{\mathbf{f}} \tag{98}$$

from which one derives

$$\frac{\mathrm{d}\hat{\mathbf{f}}}{\mathrm{d}t} = \frac{\mathrm{d}}{\mathrm{d}t}\frac{\mathbf{f}}{|\mathbf{f}|} = \frac{\dot{\mathbf{f}} - \hat{\mathbf{f}}^T\dot{\mathbf{f}}\hat{\mathbf{f}}}{|\mathbf{f}|} = \frac{\dot{\mathbf{f}} - \hat{\mathbf{f}}\hat{\mathbf{f}}^T\dot{\mathbf{f}}}{|\mathbf{f}|} = \frac{\mathbf{P}_\mathbf{f}\dot{\mathbf{f}}}{|\mathbf{f}|} \tag{99}$$

where

$$\mathbf{P}_\mathbf{f} = \mathbf{I} - \hat{\mathbf{f}}\hat{\mathbf{f}}^T \tag{100}$$

where $\mathbf{I}$ is the identity matrix. By inspection, one notes that pre-multiplication of a vector by the matrix $\mathbf{P}_\mathbf{f}$ always yields the component of that vector that is perpendicular to $\mathbf{f}$.

By using the above relations, one calculates the final relation that

$$\frac{\mathrm{d}}{\mathrm{d}t}\mathbf{P}_\mathbf{f}\mathbf{g} = -\frac{1}{|\mathbf{f}|}\left[\mathbf{P}_\mathbf{f}\dot{\mathbf{f}}\hat{\mathbf{f}}^T + \hat{\mathbf{f}}\dot{\mathbf{f}}^T\mathbf{P}_\mathbf{f}\right]\mathbf{g} + \mathbf{P}_\mathbf{f}\dot{\mathbf{g}} \tag{101}$$

B ECEF acceleration

This section relates the equations of motion of a satellite in an Earth-Centered, Earth-Fixed (ECEF) coordinate system to those in an Earth-Centered Inertial (ECI) coordinate system. These relations play a role in propagating

the orbit of a satellite since the acceleration of the satellite (derived from the egm96 gravitational potential in this document) has nothing to do with the rotation of the planet. On the other hand, SAR imaging of the ground, which rotates underneath the satellite, is most readily described in a coordinate system common both to the ground and the satellite (an ECEF system). This means that we prefer satellite position, velocity, acceleration, and the rate of change of acceleration in an ECEF coordinate system. In essence, the inertial gravitational acceleration needs to be properly interpreted in an ECEF coordinate system. We then propagate the satellite orbit in an ECEF coordinate system.

Define the relation between ECEF space and inertial space as

$$\mathbf{x}_e(t) = \mathbf{M}(t)\mathbf{x}_i(t), \tag{102}$$

and

$$\mathbf{x}_i(t) = \mathbf{M}^T(t)\mathbf{x}_e(t), \tag{103}$$

where

$$\mathbf{M}(t) = \begin{bmatrix} \cos\omega_e t & -\sin\omega_e t & 0 \\ \sin\omega_e t & \cos\omega_e t & 0 \\ 0 & 0 & 1 \end{bmatrix}, \tag{104}$$

where ω_e is the rotation rate of the earth. Calculation of derivatives yields

$$\dot{\mathbf{M}}(t) = \omega_e \begin{bmatrix} -\sin\omega_e t & -\cos\omega_e t & 0 \\ \cos\omega_e t & -\sin\omega_e t & 0 \\ 0 & 0 & 0 \end{bmatrix}, \tag{105}$$

$$\ddot{\mathbf{M}}(t) = -\omega_e^2 \begin{bmatrix} \cos\omega_e t & -\sin\omega_e t & 0 \\ \sin\omega_e t & \cos\omega_e t & 0 \\ 0 & 0 & 0 \end{bmatrix}, \tag{106}$$

and

$$\dddot{\mathbf{M}}(t) = -\omega_e^3 \begin{bmatrix} -\sin\omega_e t & -\cos\omega_e t & 0 \\ \cos\omega_e t & -\sin\omega_e t & 0 \\ 0 & 0 & 0 \end{bmatrix}. \tag{107}$$

To simplfy notation, let

$$\mathbf{I}_2 = \begin{bmatrix} 1 & 0 & 0 \\ 0 & 1 & 0 \\ 0 & 0 & 0 \end{bmatrix} \tag{108}$$

and

$$\mathbf{Q}_2 = \begin{bmatrix} 0 & -1 & 0 \\ 1 & 0 & 0 \\ 0 & 0 & 0 \end{bmatrix}. \tag{109}$$

By direct calculation

$$\mathbf{Q}_2\mathbf{Q}_2 = -\mathbf{I}_2 \tag{110}$$

For use later, we compute the following

$$\dot{\mathbf{M}}(t)\mathbf{M}^T(t) = \omega_e\mathbf{Q}_2 \tag{111}$$
$$\ddot{\mathbf{M}}(t)\mathbf{M}^T(t) = -\omega_e^2\mathbf{I}_2 \tag{112}$$
$$\dddot{\mathbf{M}}(t)\mathbf{M}^T(t) = -\omega_e^3\mathbf{Q}_2 \tag{113}$$
$$\tag{114}$$

B.1 ECEF equations of motion

With the previous material, one computes

$$\dot{\mathbf{x}}_e(t) = \dot{\mathbf{M}}(t)\mathbf{x}_i(t) + \mathbf{M}(t)\dot{\mathbf{x}}_i(t) \tag{115}$$
$$\ddot{\mathbf{x}}_e(t) = \ddot{\mathbf{M}}(t)\mathbf{x}_i(t) + 2\dot{\mathbf{M}}(t)\dot{\mathbf{x}}_i(t) + \mathbf{M}(t)\ddot{\mathbf{x}}_i(t) \tag{116}$$
$$\dddot{\mathbf{x}}_e(t) = \dddot{\mathbf{M}}(t)\mathbf{x}_i(t) + 3\ddot{\mathbf{M}}(t)\dot{\mathbf{x}}_i(t) + 3\dot{\mathbf{M}}(t)\ddot{\mathbf{x}}_i(t) + \mathbf{M}(t)\dddot{\mathbf{x}}_i(t) \tag{117}$$

From the first expression

$$\begin{aligned} \mathbf{M}^T(t)\dot{\mathbf{x}}_e(t) &= \mathbf{M}^T(t)\dot{\mathbf{M}}(t)\mathbf{M}^T(t)\mathbf{x}_e(t) + \dot{\mathbf{x}}_i(t) \\ &= \omega_e\mathbf{M}^T(t)\mathbf{Q}_2\mathbf{x}_e(t) + \dot{\mathbf{x}}_i(t) \end{aligned} \tag{118}$$

so that

$$\dot{\mathbf{x}}_i(t) = \mathbf{M}^T(t)\left[\dot{\mathbf{x}}_e(t) - \omega_e\mathbf{Q}_2\mathbf{x}_e(t)\right] \tag{119}$$

Substitution of this equivalence into the second expression above yields

$$\begin{aligned} \ddot{\mathbf{x}}_e(t) &= \ddot{\mathbf{M}}(t)\mathbf{M}^T(t)\mathbf{x}_e(t) + 2\dot{\mathbf{M}}(t)\mathbf{M}^T(t)\left[\dot{\mathbf{x}}_e(t) - \omega_e\mathbf{Q}_2\mathbf{x}_e(t)\right] + \mathbf{M}(t)\ddot{\mathbf{x}}_i(t) \\ &= -\omega_e^2\mathbf{I}_2\mathbf{x}_e(t) + 2\omega_e\mathbf{Q}_2\left[\dot{\mathbf{x}}_e(t) - \omega_e\mathbf{Q}_2\mathbf{x}_e(t)\right] + \mathbf{M}(t)\ddot{\mathbf{x}}_i(t) \\ &= -\omega_e^2\mathbf{I}_2\mathbf{x}_e(t) + 2\omega_e\mathbf{Q}_2\dot{\mathbf{x}}_e(t) + 2\omega_e^2\mathbf{I}_2\mathbf{x}_e(t) + \mathbf{M}(t)\ddot{\mathbf{x}}_i(t) \\ &= \omega_e^2\mathbf{I}_2\mathbf{x}_e(t) + 2\omega_e\mathbf{Q}_2\dot{\mathbf{x}}_e(t) + \mathbf{M}(t)\ddot{\mathbf{x}}_i(t) \end{aligned} \tag{120}$$

and substitution into the third expression yields

$$\begin{aligned}\dddot{\mathbf{x}}_e(t) &= \dddot{\mathbf{M}}(t)\mathbf{M}^T(t)\mathbf{x}_e(t) + 3\ddot{\mathbf{M}}(t)\mathbf{M}^T(t)\left[\dot{\mathbf{x}}_e(t) - \omega_e\mathbf{Q}_2\mathbf{x}_e(t)\right] \\ &\quad + 3\dot{\mathbf{M}}(t)\ddot{\mathbf{x}}_i(t) + \mathbf{M}(t)\dddot{\mathbf{x}}_i(t) \\ &= -\omega_e^3\mathbf{Q}_2\mathbf{x}_e(t) - 3\omega_e^2\mathbf{I}_2\left[\dot{\mathbf{x}}_e(t) - \omega_e\mathbf{Q}_2\mathbf{x}_e(t)\right] + 3\dot{\mathbf{M}}(t)\ddot{\mathbf{x}}_i(t) + \mathbf{M}(t)\dddot{\mathbf{x}}_i(t) \\ &= 2\omega_e^3\mathbf{Q}_2\mathbf{x}_e(t) - 3\omega_e^2\mathbf{I}_2\dot{\mathbf{x}}_e(t) + 3\dot{\mathbf{M}}(t)\ddot{\mathbf{x}}_i(t) + \mathbf{M}(t)\dddot{\mathbf{x}}_i(t)\end{aligned} \tag{121}$$

B.2 Rate of change of acceleration

This subsection computes the rate of change of acceleration of a satellite in an intertial Earth-Centered coordinate system. Further, because the egm96 gravitational potential, (97), is defined using spherical-polar coordinates, this subsection also demonstrates how to convert the gradient of this potential into a Cartesian representation. The ECEF rate of change of acceleration is then given by the derivative of this acceleration with respect to time and one then acquires the ECEF equations of motion by substituting the two computed quantities into (120) and (121).

The gravitational potential, $U(r, \phi, \lambda)$, is defined in (97), and the gradient of this quantity defines the gravitational acceleration. We convert the gradient in spherical-polar coordinates to a graident in Cartesian coordinates, x, y, z, through

$$\begin{aligned}\ddot{\mathbf{x}}_i(t) = \vec{\nabla}_{x,y,z}U &= \begin{bmatrix} \frac{\partial r}{\partial x} & \frac{\partial \phi}{\partial x} & \frac{\partial \lambda}{\partial x} \\ \frac{\partial r}{\partial y} & \frac{\partial \phi}{\partial y} & \frac{\partial \lambda}{\partial y} \\ \frac{\partial r}{\partial z} & \frac{\partial \phi}{\partial z} & \frac{\partial \lambda}{\partial z} \end{bmatrix} \begin{bmatrix} \frac{\partial U}{\partial r} \\ \frac{\partial U}{\partial \phi} \\ \frac{\partial U}{\partial \lambda} \end{bmatrix} \\ &= \left[\frac{\partial(r,\phi,\lambda)}{\partial(x,y,z)}\right]^T \vec{\nabla}_{r,\phi,\lambda}U.\end{aligned} \tag{122}$$

Note that, although the above equation does explicitely show a time dependence on the left side, the time variable has been supressed on the right to allow for more compact notation. In actual fact, the position coordinates do depend on time. More explicitely, the position of a body is given by $x(t), y(t), z(t)$. Thus, to compute the derivative of the acceleration, one must compute

$$\dddot{\mathbf{x}}_i(t) = \frac{\mathrm{d}\vec{\nabla}_{x,y,z}U}{\mathrm{d}t} = \begin{bmatrix} \frac{\partial^2 U}{\partial x^2} & \frac{\partial^2 U}{\partial y \partial x} & \frac{\partial^2 U}{\partial z \partial x} \\ \frac{\partial^2 U}{\partial x \partial y} & \frac{\partial^2 U}{\partial y^2} & \frac{\partial^2 U}{\partial z \partial y} \\ \frac{\partial^2 U}{\partial x \partial z} & \frac{\partial^2 U}{\partial y \partial z} & \frac{\partial^2 U}{\partial z^2} \end{bmatrix} \begin{bmatrix} \frac{\mathrm{d}x}{\mathrm{d}t} \\ \frac{\mathrm{d}y}{\mathrm{d}t} \\ \frac{\mathrm{d}z}{\mathrm{d}t} \end{bmatrix} \tag{123}$$

A representative component of the matrix in the above may be written as

$$\begin{aligned}
\frac{\partial^2 U}{\partial x_i \partial x_j} &= \frac{\partial \frac{\partial U}{\partial x_j}}{\partial x_i} \\
&= \frac{\partial}{\partial x_i}\begin{bmatrix} \frac{\partial r}{\partial x_j} & \frac{\partial \phi}{\partial x_j} & \frac{\partial \lambda}{\partial x_j} \end{bmatrix}\begin{bmatrix} \frac{\partial U}{\partial r} \\ \frac{\partial U}{\partial \phi} \\ \frac{\partial U}{\partial \lambda} \end{bmatrix} \\
&= \begin{bmatrix} \frac{\partial^2 r}{\partial x_i \partial x_j} & \frac{\partial^2 \phi}{\partial x_i \partial x_j} & \frac{\partial^2 \lambda}{\partial x_i \partial x_j} \end{bmatrix}\begin{bmatrix} \frac{\partial U}{\partial r} \\ \frac{\partial U}{\partial \phi} \\ \frac{\partial U}{\partial \lambda} \end{bmatrix} + \begin{bmatrix} \frac{\partial r}{\partial x_j} & \frac{\partial \phi}{\partial x_j} & \frac{\partial \lambda}{\partial x_j} \end{bmatrix}\begin{bmatrix} \frac{\partial^2 U}{\partial x_j \partial r} \\ \frac{\partial^2 U}{\partial x_i \partial \phi} \\ \frac{\partial^2 U}{\partial x_i \partial \lambda} \end{bmatrix} \\
&= \begin{bmatrix} \frac{\partial U}{\partial r} & \frac{\partial U}{\partial \phi} & \frac{\partial U}{\partial \lambda} \end{bmatrix}\begin{bmatrix} \frac{\partial^2 r}{\partial x_i \partial x_j} \\ \frac{\partial^2 \phi}{\partial x_i \partial x_j} \\ \frac{\partial^2 \lambda}{\partial x_i \partial x_j} \end{bmatrix} + \begin{bmatrix} \frac{\partial r}{\partial x_j} & \frac{\partial \phi}{\partial x_j} & \frac{\partial \lambda}{\partial x_j} \end{bmatrix}\begin{bmatrix} \frac{\partial^2 U}{\partial r^2} & \frac{\partial^2 U}{\partial \phi \partial r} & \frac{\partial^2 U}{\partial \lambda \partial r} \\ \frac{\partial^2 U}{\partial r \partial \phi} & \frac{\partial^2 U}{\partial \phi^2} & \frac{\partial^2 U}{\partial \lambda \partial \phi} \\ \frac{\partial^2 U}{\partial r \partial \lambda} & \frac{\partial^2 U}{\partial \phi \partial \lambda} & \frac{\partial^2 U}{\partial \lambda^2} \end{bmatrix}\begin{bmatrix} \frac{\partial r}{\partial x_i} \\ \frac{\partial \phi}{\partial x_i} \\ \frac{\partial \lambda}{\partial x_i} \end{bmatrix}
\end{aligned} \tag{124}$$

One can consolidate all the terms into matrix form via

$$\begin{aligned}
\dddot{\mathbf{x}}_i(t) = \frac{\mathrm{d}\vec{\nabla}_{x,y,z} U}{\mathrm{d}t} = \\
&\begin{bmatrix} \frac{\partial U}{\partial r} & \frac{\partial U}{\partial \phi} & \frac{\partial U}{\partial \lambda} & 0 & 0 & 0 & 0 & 0 & 0 \\ 0 & 0 & 0 & \frac{\partial U}{\partial r} & \frac{\partial U}{\partial \phi} & \frac{\partial U}{\partial \lambda} & 0 & 0 & 0 \\ 0 & 0 & 0 & 0 & 0 & 0 & \frac{\partial U}{\partial r} & \frac{\partial U}{\partial \phi} & \frac{\partial U}{\partial \lambda} \end{bmatrix}\begin{bmatrix} \frac{\partial^2 r}{\partial x \partial x} & \frac{\partial^2 r}{\partial x \partial y} & \frac{\partial^2 r}{\partial x \partial z} \\ \frac{\partial^2 \phi}{\partial x \partial x} & \frac{\partial^2 \phi}{\partial x \partial y} & \frac{\partial^2 \phi}{\partial x \partial z} \\ \frac{\partial^2 \lambda}{\partial x \partial x} & \frac{\partial^2 \lambda}{\partial x \partial y} & \frac{\partial^2 \lambda}{\partial x \partial z} \\ \frac{\partial^2 r}{\partial y \partial x} & \frac{\partial^2 r}{\partial y \partial y} & \frac{\partial^2 r}{\partial y \partial z} \\ \frac{\partial^2 \phi}{\partial y \partial x} & \frac{\partial^2 \phi}{\partial y \partial y} & \frac{\partial^2 \phi}{\partial y \partial z} \\ \frac{\partial^2 \lambda}{\partial y \partial x} & \frac{\partial^2 \lambda}{\partial y \partial y} & \frac{\partial^2 \lambda}{\partial y \partial z} \\ \frac{\partial^2 r}{\partial z \partial x} & \frac{\partial^2 r}{\partial z \partial y} & \frac{\partial^2 r}{\partial z \partial z} \\ \frac{\partial^2 \phi}{\partial z \partial x} & \frac{\partial^2 \phi}{\partial z \partial y} & \frac{\partial^2 \phi}{\partial z \partial z} \\ \frac{\partial^2 \lambda}{\partial z \partial x} & \frac{\partial^2 \lambda}{\partial z \partial y} & \frac{\partial^2 \lambda}{\partial z \partial z} \end{bmatrix}\begin{bmatrix} \frac{\mathrm{d}x}{\mathrm{d}t} \\ \frac{\mathrm{d}y}{\mathrm{d}t} \\ \frac{\mathrm{d}z}{\mathrm{d}t} \end{bmatrix} \\
+ &\begin{bmatrix} \frac{\partial r}{\partial x} & \frac{\partial \phi}{\partial x} & \frac{\partial \lambda}{\partial x} \\ \frac{\partial r}{\partial y} & \frac{\partial \phi}{\partial y} & \frac{\partial \lambda}{\partial y} \\ \frac{\partial r}{\partial z} & \frac{\partial \phi}{\partial z} & \frac{\partial \lambda}{\partial z} \end{bmatrix}\begin{bmatrix} \frac{\partial^2 U}{\partial r^2} & \frac{\partial^2 U}{\partial \phi \partial r} & \frac{\partial^2 U}{\partial \lambda \partial r} \\ \frac{\partial^2 U}{\partial r \partial \phi} & \frac{\partial^2 U}{\partial \phi^2} & \frac{\partial^2 U}{\partial \lambda \partial \phi} \\ \frac{\partial^2 U}{\partial r \partial \lambda} & \frac{\partial^2 U}{\partial \phi \partial \lambda} & \frac{\partial^2 U}{\partial \lambda^2} \end{bmatrix}\begin{bmatrix} \frac{\partial r}{\partial x} & \frac{\partial r}{\partial y} & \frac{\partial r}{\partial z} \\ \frac{\partial \phi}{\partial x} & \frac{\partial \phi}{\partial y} & \frac{\partial \phi}{\partial z} \\ \frac{\partial \lambda}{\partial x} & \frac{\partial \lambda}{\partial y} & \frac{\partial \lambda}{\partial z} \end{bmatrix}\begin{bmatrix} \frac{\mathrm{d}x}{\mathrm{d}t} \\ \frac{\mathrm{d}y}{\mathrm{d}t} \\ \frac{\mathrm{d}z}{\mathrm{d}t} \end{bmatrix}
\end{aligned} \tag{125}$$

C Derivation of the arclength-paremterized range function

The range between the satellite and a target plays a critical role in SAR processing. This section presents an arclength parameterized expression for this range function. The final approximation of the section, (139), yields a version of the function that only weakly depends on the expansion point used to describe the satellite orbit.

For every scatterer at point $\mathbf{x}$, there is an arclength value, $s_{\mathbf{x}}$, such that $\mathbf{c}_p(s_{\mathbf{x}}) - \mathbf{x}$ is perpendicular to $\mathbf{c}_p'(s_{\mathbf{x}})$. Further, $\mathbf{x}$ can be completely determined by

$$\mathbf{x} = \mathbf{c}_p(s_{\mathbf{x}}) + r\cos\phi\mathbf{N}(s_{\mathbf{x}}) + r\sin\phi\mathbf{B}(s_{\mathbf{x}}), \tag{126}$$

where $r = |\mathbf{c}_p(s_{\mathbf{x}}) - \mathbf{x}|$ and $r\cos\phi = [\mathbf{x} - \mathbf{c}_p(s_{\mathbf{x}})] \cdot \mathbf{N}(s_{\mathbf{x}})$.

One computes that

$$\begin{aligned}
\mathbf{c}_p(s) - \mathbf{x} &= \mathbf{c}_p(s) - \mathbf{c}_p(s_{\mathbf{x}}) - r\cos\phi\mathbf{N}(s_{\mathbf{x}}) - r\sin\phi\mathbf{B}(s_{\mathbf{x}}) \\
&= (s - s_{\mathbf{x}})\mathbf{T}_0 + \frac{(s-s_0)^2 - (s_{\mathbf{x}} - s_0)^2}{2}\kappa_0\mathbf{N}_0 \\
&+ \frac{(s-s_0)^3 - (s_{\mathbf{x}} - s_0)^3}{6}[-\kappa_0^2\mathbf{T}_0 + \dot{\kappa}_0\mathbf{N}_0 + \kappa_0\tau_0\mathbf{B}_0] \\
&- r\cos\phi\mathbf{N}(s_{\mathbf{x}}) - r\sin\phi\mathbf{B}(s_{\mathbf{x}}) \\
&= (a-b)\left[\mathbf{T}_0 + \frac{a+b}{2}\kappa_0\mathbf{N}_0 + \frac{a^2+ab+b^2}{6}[-\kappa_0^2\mathbf{T}_0 + \dot{\kappa}_0\mathbf{N}_0 + \kappa_0\tau_0\mathbf{B}_0]\right] \\
&- r\cos\phi\mathbf{N}(s_{\mathbf{x}}) - r\sin\phi\mathbf{B}(s_{\mathbf{x}})
\end{aligned} \tag{127}$$

where

$$a = (s - s_0) \tag{128}$$

$$b = (s_{\mathbf{x}} - s_0) \tag{129}$$

More succinctly, one can write

$$\mathbf{c}_p(s) - \mathbf{x} = (a-b)(\alpha_T\mathbf{T}_0 + \alpha_N\mathbf{N}_0 + \alpha_B\mathbf{B}_0) - r\cos\phi\mathbf{N}(s_{\mathbf{x}}) - r\sin\phi\mathbf{B}(s_{\mathbf{x}}) \tag{130}$$

where

$$\alpha_T = 1 - \kappa_0^2 \frac{a^2 + ab + b^2}{6} \tag{131}$$

$$\alpha_N = \kappa_0 \frac{a+b}{2} + \dot{\kappa}_0 \frac{a^2 + ab + b^2}{6} \tag{132}$$

$$\alpha_B = \kappa_0 \tau_0 \frac{a^2 + ab + b^2}{6} \tag{133}$$

From the Frenet-Serret equations, one can make the approximation that

$$r\cos\phi \mathbf{N}(s_{\mathbf{x}}) \approx r\cos\phi \mathbf{N}_0 + (s_{\mathbf{x}} - s_0) r\cos\phi(-\kappa_0 \mathbf{T}_0 + \tau_0 \mathbf{B}_0) \tag{134}$$

$$r\sin\phi \mathbf{B}(s_{\mathbf{x}}) \approx r\sin\phi \mathbf{B}_0 - (s_{\mathbf{x}} - s_0) r\sin\phi \tau_0 \mathbf{N}_0 \tag{135}$$

and since $s_{\mathbf{x}} - s_0 = b$, the range expression can be written as

$$\begin{aligned} \mathbf{c}_p(s) - \mathbf{x} = &[(a-b)\alpha_T + br\kappa_0 \cos\phi]\mathbf{T}_0 \\ &+ [(a-b)\alpha_N - r\cos\phi + br\tau_0 \sin\phi]\mathbf{N}_0 \\ &+ [(a-b)\alpha_B - r\sin\phi - br\tau_0 \cos\phi]\mathbf{B}_0 \end{aligned} \tag{136}$$

The computation of square of the above expression yields a polynomial in $(a-b) = (s - s_{\mathbf{x}})$ (after using sagemath),

$$|\mathbf{c}_p(s) - \mathbf{x}|^2 = \sum_{k=0^5} a_k (s - s_{\mathbf{x}})^k \tag{137}$$

with the following coefficients

$$
\begin{aligned}
a_0 &= b^2\kappa_0^2 r^2\cos^2\phi + b^2 r^2\tau_0^2 + r^2 \\
a_1 &= \frac{2b^2\tau_0 r}{3}(b\dot{\kappa}_0 + 2\kappa_0)\sin\phi - \frac{2b^2 r}{3}(b\kappa_0\tau_0^2 + b\kappa_0^3 + \dot{\kappa}_0)\cos\phi \\
a_2 &= 1 - [\kappa_0 + b\dot{\kappa}_0 + b^2(\kappa_0^3 + \kappa_0\tau_0^2)]r\cos\phi + b^2\dot{\kappa}_0\tau_0 r\sin\phi \\
&\quad + \frac{b^4}{9}(\kappa_0^4 + \kappa_0^2\tau_0^2 + \dot{\kappa}_0^2) + \frac{b^2\kappa_0}{3}(\kappa_0 + 2b\dot{\kappa}_0) \\
a_3 &= -\frac{r}{3}(\kappa_0\tau_0\sin\phi + \dot{\kappa}_0\cos\phi) + \frac{b^3}{3}(\kappa_0^4 + \kappa_0^2\tau_0^2 + \dot{\kappa}_0^2) + \frac{4b^2}{3}\kappa_0\dot{\kappa}_0 \\
&\quad + \frac{br}{3}[\dot{\kappa}_0\tau_0\sin\phi - (\kappa_0\tau_0^2 + \kappa_0^3)\cos\phi] \\
a_4 &= -\frac{\kappa_0^2}{12} + \frac{13b^2}{36}(\kappa_0^4 + \kappa_0^2\tau_0^2 + \dot{\kappa}_0^2) + \frac{5b\kappa_0\dot{\kappa}_0}{6} \\
a_5 &= \frac{b}{6}(\kappa_0^4 + \kappa_0^2\tau_0^2 + \dot{\kappa}_0^2 + \kappa\dot{\kappa}_0) \\
a_6 &= \frac{1}{36}(\kappa_0^4 + \kappa_0^2\tau_0^2 + \dot{\kappa}_0^2)
\end{aligned}
\tag{138}
$$

In the region of the chosen point of expansion, s_0, b evaluates to a relatively small number, thus, one can make the approximation that

$$
\begin{aligned}
a_0 &= r^2 \\
a_1 &= 0 \\
a_2 &= 1 - \kappa_0 r\cos\phi \\
a_3 &= -\frac{r}{3}(\kappa_0\tau_0\sin\phi + \dot{\kappa}_0\cos\phi) \\
a_4 &= -\frac{\kappa_0^2}{12} \\
a_5 &= 0 \\
a_6 &= 0
\end{aligned}
\tag{139}
$$

D Numerical implementation of the Stolz interpolation

This section outlines an approach to support numerical implementation of the proposed, generalized Stolz interpolation. Because the generalized Stolz

interpolation points do not have a closed form as they do in, for instance, [8, 11], this section presents a numerical approach. There is nothing particularly insightful about the proposed algorithm; in fact, this section aims to present an approach that avoids confusion and facilitates numerical implementation.

So, to begin, let

$$x = \frac{r \tan \theta_s}{\sqrt{a_2}}. \tag{140}$$

This means that

$$\sin \theta_s = \frac{x\sqrt{a_2}}{\sqrt{r^2 + a_2 x^2}} \tag{141}$$

$$\cos \theta_s = \frac{r}{\sqrt{r^2 + a_2 x^2}}, \tag{142}$$

which means that

$$\frac{x\sqrt{a_2}}{\sqrt{r^2 + a_2 x^2}} \left[g(-x) - \frac{a_3 \sqrt{a_2} x}{2g^2(-x)} + \frac{a_4 a_2 x^2}{g^3(-x)} \right] = \frac{k_s}{k_r}. \tag{143}$$

Now, from (69), when one makes the (Stolt interpolation) change of variables

$$k_{r_s} = k_r \sec \theta_s - k_s \frac{\tan \theta_s}{g\left(\frac{-r \tan \theta_s}{\sqrt{a_2}}\right)}, \tag{144}$$

which leads to the relation that

$$k_r = \frac{r k_{r_s}}{\sqrt{r^2 + a_2 x^2}} + \frac{k_s x \sqrt{a_2}}{g(-x)\sqrt{r^2 + a_2 x^2}}. \tag{145}$$

D.1 Simplification for iterative root-finding

In the opinion of the authors, implementation of the Stolz interpolation (into computer code) benefits from defining the following function

$$\psi(x; l, m, n) = \frac{x^l}{(r^2 + a_2 x^2)^m g^n(-x)} \tag{146}$$

This function posesses the following derivative which proves useful in applying a Newton numerical, iterative, root-finding procedure,

$$\frac{\mathrm{d}\psi(x; l, m, n)}{\mathrm{d}x} = \psi(x; l-1, m, n) \left(l - m \frac{2a_2 x^2}{r^2 + a_2 x^2} + n \frac{a_3/2 - a_4 x}{g^2(-x)} \right) \tag{147}$$

With the aforementioned definition,

$$k_r = rk_{r_s}\psi(x;0,1/2,0) + k_s\sqrt{a_2}\psi(x;1,1/2,1), \tag{148}$$

and, when this is substituted into (66), along with the realtions in (141) and (142), one obtains

$$\begin{aligned}&\sqrt{a_2}rk_{r_s}\psi(x;1,1,-1) + a_2k_s\psi(x;2,1,0) - \frac{rk_{r_s}a_2a_3}{2}\psi(x;2,1,2)\\ &+\left(rk_{r_s}a_4 - \frac{a_3k_s}{2}\right)a_2^{3/2}\psi(x;3,1,3) + a_2^2a_4k_s\psi(x;4,1,4) = k_s\end{aligned} \tag{149}$$

Equation 149 permits numerical computation of x given values for k_s and k_{r_s}. This computed value for x can be inserted into 148 to provide the particular value of k_r at which the data need to be estimated (through interpolation).

E MIMO configuration

This section demonstrates how subarrays of a uniform phased array antenna can be combined to yield signals of the form of (37). In the configuration described below, Transmit/Receive T/R modules form the basic element of the phased array.

As illustrated in Figure 8, assume that every transmission, from every element, is received and summed independently (i.e. assume superpostiion applies). Assume further that signals are transmitted at time τ, but with different delays on transmission (programmed delays) for each T/R module and that the echoes of these signals are received at time $\tau + 2r(s)/c$, but with different Rx delays for each T/R module (programmed delays)

Now, the time delay to irradiate a target depends on the position of the transmitter and the location of the target. In the model, we denote the target position as $s_{\mathbf{x}}$ and the position of each transmitter and receiver as $\mathbf{T}_{x_{n'}}$, $n' \in \{0, N'-1\}$ and $\mathbf{R}_{x_{m'}}$, $m' \in \{0, M'-1\}$, respectively. We also denote the transmitted waveform as

$$z(\tau) = p(\tau)e^{i\omega_0\tau}, \tag{150}$$

where $p(\tau)$ is some baseband waveform. With this notation, and with transmit and receive delays given by $\delta_{T_{n'}}$ and $\delta_{R_{m'}}$, respectively, the far field delay

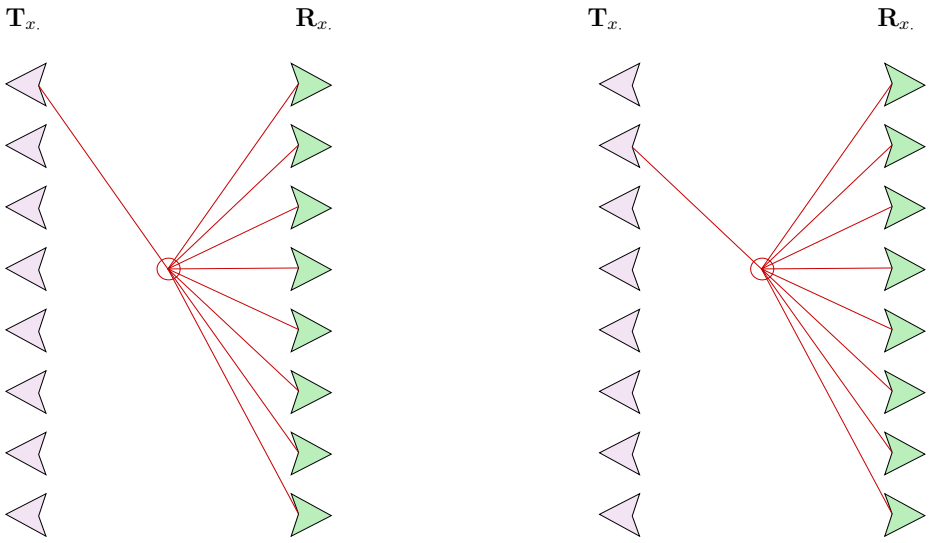

Figure 8: Configuration of transmit and receive. Each transmitted signal is received by all receivers

for a transmit/receive pair is given by

$$\delta_{m'n'}(s) = \frac{2r(s,\mathbf{x})}{c} + \delta_{T_{n'}} + \delta_{R_{n'}} + \frac{\mathbf{T}_{x_{n'}} \cdot \hat{\mathbf{r}}(s,\mathbf{x})}{c} + \frac{\mathbf{R}_{x_{m'}} \cdot \hat{\mathbf{r}}(s,\mathbf{x})}{c} \tag{151}$$

and the return signal is given by

$$z_{mn}(\tau, s) = \mathrm{A}_{T_{n'}} \mathrm{A}_{R_{m'}} z[\tau - \delta_{m'n'}(s)]. \tag{152}$$

Through the principle of superposition, the system measured signal is given by

$$\begin{aligned} z_s(\tau, s) &= \sum_{m',n'} z_{m'n'}(\tau, s) \\ &= \sum_{m',n'} \mathrm{A}_{T_{n'}} \mathrm{A}_{R_{m'}} z[\tau - \delta_{m'n'}(s)]. \end{aligned} \tag{153}$$

In the fast-time frequency domain, this signal can be written as

$$\begin{aligned} Z_s(\omega', s) &= \sum_{m',n'} \mathrm{A}_{T_{n'}} \mathrm{A}_{R_{m'}} Z(\omega') e^{-i\omega' \delta_{m'n'}(s)} \\ &= Z(\omega') e^{-i\omega' \frac{2r(s,\mathbf{x})}{c}} \sum_{n'} \mathrm{A}_{T_{n'}} e^{-i\omega' [\delta_{T_{n'}} + \frac{\mathbf{T}_{x_{n'}} \cdot \hat{\mathbf{r}}(s,\mathbf{x})}{c}]} \\ &\cdot \sum_{m'} \mathrm{A}_{R_{m'}} e^{-i\omega' [\delta_{R_{m'}} + \frac{\mathbf{R}_{x_{m'}} \cdot \hat{\mathbf{r}}(s,\mathbf{x})}{c}]}, \end{aligned} \tag{154}$$

where $\omega' = \omega + \omega_0$.

Suppose that $\mathbf{T}_{x_{n'}} = n'\mathbf{b}$ and that $\mathbf{R}_{x_{m'}} = m'\mathbf{b}$, i.e. a uniformly spaced array, and that the timing delays are chosen such that $\delta_{T_{n'}} = -n'\mathbf{b} \cdot \mathbf{u}_n / c$ and $\delta_{R_{m'}} = -m'\mathbf{b} \cdot \mathbf{u}_n / c$ for some given look vector $\mathbf{u}_n$. In this case, the signal becomes

$$\begin{aligned} Z_s(\omega', s) &= Z(\omega') e^{-i\omega' \frac{2r(s,\mathbf{x})}{c}} \sum_{n'} \mathrm{A}_{T_{n'}} e^{-i\omega' \frac{n'}{c} \mathbf{b} \cdot [-\mathbf{u}_n + \hat{\mathbf{r}}(s,\mathbf{x})]} \\ &\cdot \sum_{m'} \mathrm{A}_{R_{m'}} e^{-i\omega' \frac{m'}{c} \mathbf{b} \cdot [-\mathbf{u}_n + \hat{\mathbf{r}}(s,\mathbf{x})]} \end{aligned} \tag{155}$$

Further, suppose that the weights, $\mathrm{A}_{T_{n'}}$ and $\mathrm{A}_{R_{m'}}$, are such that $\exists n'_n, m'_n$ with the properties that both

$$\sum_{n'} \mathrm{A}_{T_{n'}} e^{-i\omega' \frac{n' - n'_n}{c} \mathbf{b} \cdot [-\mathbf{u}_n + \hat{\mathbf{r}}(s,\mathbf{x})]} \tag{156}$$

and

$$\sum_{m'} \mathrm{A}_{R_{m'}} e^{-i\omega' \frac{m' - m'_n}{c} \mathbf{b} \cdot [-\mathbf{u}_n + \hat{\mathbf{r}}(s,\mathbf{x})]} \tag{157}$$

are real $\forall \omega'$. As a particular example, if $\mathrm{A}_{T_{n'}} = A_{T_x}$, a constant, for $n' \in \{n'_0, n'_0+1, n'_0+2, \ldots, n'_0+N'-1\}$, then $n'_n = n'_0 + N'/2$. With this condition,

$$\begin{aligned} Z_s(\omega', s) = Z(\omega') e^{-i\omega' \frac{2r(s,\mathbf{x})}{c}} e^{-i\omega' \frac{n'_n}{c} \mathbf{b} \cdot [-\mathbf{u}_n + \hat{\mathbf{r}}(s,\mathbf{x})]} e^{-i\omega' \frac{m'_n}{c} \mathbf{b} \cdot [-\mathbf{u}_n + \hat{\mathbf{r}}(s,\mathbf{x})]} \\ \sum_{n'} \mathrm{A}_{T_{n'}} e^{-i\omega' \frac{n' - n'_n}{c} \mathbf{b} \cdot [-\mathbf{u}_n + \hat{\mathbf{r}}(s,\mathbf{x})]} \sum_{m'} \mathrm{A}_{R_{m'}} e^{-i\omega' \frac{m' - m'_n}{c} \mathbf{b} \cdot [-\mathbf{u}_n + \hat{\mathbf{r}}(s,\mathbf{x})]} \end{aligned} \tag{158}$$

With $\omega'/c = k_r/2$, let

$$\mathbf{p}_n(s) = \frac{n'_n \mathbf{b} + m'_n \mathbf{b}}{2}, \tag{159}$$

and define

$$\begin{aligned}\mathrm{D}_n[k_r, \hat{\mathbf{r}}(s,\mathbf{x})] = &\sum_{n'} \mathrm{A}_{T_{n'}} e^{-ik_r \frac{n'-n'_n}{2}\mathbf{b}\cdot[-\mathbf{u}_n+\hat{\mathbf{r}}(s,\mathbf{x})]} \\ &\sum_{m'} \mathrm{A}_{R_{m'}} e^{-ik_r \frac{m'-m'_n}{2}\mathbf{b}\cdot[-\mathbf{u}_n+\hat{\mathbf{r}}(s,\mathbf{x})]}.\end{aligned} \tag{160}$$

Then,

$$Z_s(k_r, s) = Z(k_r) e^{-ik_r r(s,\mathbf{x})} e^{-ik_r \mathbf{p}_n(s)\cdot\hat{\mathbf{r}}(s,\mathbf{x})} e^{ik_r \mathbf{p}_n(s)\cdot\mathbf{u}_n} \mathrm{D}_n[k_r, \hat{\mathbf{r}}(s,\mathbf{x})] \tag{161}$$

Finally, compute $e^{-ik_r \mathbf{p}_n(s)\cdot\mathbf{u}_n} Z_s(k_r, s)$ to obtain the expression in (45).

F Antenna pattern angles

Let us examine $\hat{\mathbf{r}}(s,\mathbf{x})\cdot\mathbf{N}(s)$ and $\hat{\mathbf{r}}(s,\mathbf{x})\cdot\mathbf{B}(s)$ by exanding these terms around $s_0, \mathbf{x}_0$. A first order expansion of the look vector yields

$$\hat{\mathbf{r}}(s,\mathbf{x}) \approx \hat{\mathbf{r}}_0 + (s-s_0)\frac{\mathbf{P}_{\mathbf{r}_0}\mathbf{T}_0}{r_0} + \frac{\mathbf{P}_{\mathbf{r}_0}(\mathbf{x}-\mathbf{x}_0)}{r_0}, \tag{162}$$

where $\mathbf{r}_0 = \mathbf{r}(s_0, \mathbf{x}_0)$.

Since $\mathbf{T}_0$ is perpendicular to $\mathbf{r}_0$, one immediately finds that $\mathbf{P}_{\mathbf{r}_0}\mathbf{T}_0 = \mathbf{T}_0$. Furthermore

$$\mathbf{x}_0 = \mathbf{c}(s_0) + r_0\cos\phi_0\mathbf{N}_0 + r_0\sin\phi_0\mathbf{B}_0, \tag{163}$$

and

$$\begin{aligned}\mathbf{x} = \mathbf{c}(s_0) + (s_\mathbf{x}-s_0)\mathbf{T}_0 + \frac{(s_\mathbf{x}-s_0)^2}{2}\kappa_0\mathbf{N}_0 + \frac{(s_\mathbf{x}-s_0)^3}{6}[-\kappa_0^2\mathbf{T}_0 + \dot{\kappa}_0\mathbf{N}_0 + \kappa_0\tau_0\mathbf{B}_0] \\ + r\cos\phi\left[\mathbf{N}_0 + (s_\mathbf{x}-s_0)\Big(-\kappa_0\mathbf{T}_0 + \tau_0\mathbf{B}_0\Big)\right] + r\sin\phi\left[\mathbf{B}_0 + (s_\mathbf{x}-s_0)\Big(-\tau_0\mathbf{N}_0\Big)\right]\end{aligned} \tag{164}$$

In the above, we have used the Frenet-Serret equations of (11) to make the approximation that

$$\mathbf{N}(s) \approx \mathbf{N}_0 + (s-s_0)\Big[-\kappa_0\mathbf{T}_0 + \tau_0\mathbf{B}_0\Big] \tag{165}$$

$$\mathbf{B}(s) \approx \mathbf{B}_0 + (s-s_0)\Big[-\tau_0\mathbf{N}_0\Big] \tag{166}$$

Now with

$$\hat{\mathbf{r}}_0 = \cos\phi_0 \mathbf{N}_0 + \sin\phi_0 \mathbf{B}_0 \tag{167}$$

one can calculate that

$$\hat{\mathbf{r}}_{0\perp} = \sin\phi_0 \mathbf{N}_0 - \cos\phi_0 \mathbf{B}_0. \tag{168}$$

By combining equations (163), (164) and (168), one arrives at the following expressions

$$\mathbf{P}_{\mathbf{r}_0}(\mathbf{x} - \mathbf{x}_0) = [\hat{\mathbf{r}}_{0\perp} \cdot (\mathbf{x} - \mathbf{x}_0)]\hat{\mathbf{r}}_{0\perp} \tag{169}$$

and

$$\begin{aligned}\hat{\mathbf{r}}_{0\perp} \cdot (\mathbf{x} - \mathbf{x}_0) \approx \frac{1}{6}(s_{\mathbf{x}} - s_0)^3[\kappa_0\tau_0\cos\phi_0 - \dot{\kappa}_0\sin\phi_0] + \frac{1}{2}\kappa(s_{\mathbf{x}} - s_0)^2\sin\phi_0 \\ - (s_{\mathbf{x}} - s_0)r\tau_0\cos(\phi - \phi_0) - r\sin(\phi - \phi_0)\end{aligned} \tag{170}$$

The only term that makes a difference in the above is $r\sin(\phi - \phi_0)$, thus

$$\frac{\mathbf{P}_{\mathbf{r}_0}(\mathbf{x} - \mathbf{x}_0)}{r_0} \approx -\frac{r}{r_0}\sin(\phi - \phi_0)\hat{\mathbf{r}}_{0\perp} \tag{171}$$

Thus, one finally arrives at

$$\begin{aligned}\hat{\mathbf{r}}(s, \mathbf{x}) &\approx \hat{\mathbf{r}}_0 + (s - s_0)\frac{\mathbf{T}_0}{r_0} + \frac{r}{r_0}\sin(\phi - \phi_0)\hat{\mathbf{r}}_{0\perp} \\ &= \cos\phi_0\mathbf{N}_0 + \sin\phi_0\mathbf{B}_0 + (s - s_0)\frac{\mathbf{T}_0}{r_0} \\ &+ \frac{r}{r_0}\sin(\phi - \phi_0)[\sin\phi_0\mathbf{N}_0 - \cos\phi_0\mathbf{B}_0] \\ &= [\cos\phi_0 + \frac{r}{r_0}\sin\phi_0\sin(\phi - \phi_0)]\mathbf{N}_0 \\ &+ [\sin\phi_0 - \frac{r}{r_0}\cos\phi_0\sin(\phi - \phi_0)]\mathbf{B}_0 \\ &+ (s - s_0)\frac{\mathbf{T}_0}{r_0}\end{aligned} \tag{172}$$

Note that in the neighbourhood of $\mathbf{x}_0$, $\sin(\phi - \phi_0) \approx \phi - \phi_0$ and $\frac{r}{r_0} \approx 1$ one arrives at the approximation that

$$\hat{\mathbf{r}}(s, \mathbf{x}) \approx \cos\phi\mathbf{N}_0 + \sin\phi\mathbf{B}_0 + (s - s_0)\frac{\mathbf{T}_0}{r_0} \tag{173}$$

Substitution of the approximations for $\mathbf{N}(s)$ and $\mathbf{B}(s)$ yields

$$\begin{aligned}\hat{\mathbf{r}}(s,\mathbf{x})\cdot\mathbf{N}(s) \approx \cos\phi_0 &+ \frac{r}{r_0}\sin\phi_0\sin(\phi-\phi_0)\\ &+ \tau_0(s-s_0)[\sin\phi_0 - \frac{r}{r_0}\cos\phi_0\sin(\phi-\phi_0)]\\ &- \kappa_0\frac{(s-s_0)^2}{r_0}\end{aligned} \tag{174}$$

and

$$\begin{aligned}\hat{\mathbf{r}}(s,\mathbf{x})\cdot\mathbf{B}(s) \approx \sin\phi_0 &- \frac{r}{r_0}\cos\phi_0\sin(\phi-\phi_0)\\ &- \tau_0(s-s_0)[\cos\phi_0 + \frac{r}{r_0}\sin\phi_0\sin(\phi-\phi_0)]\end{aligned} \tag{175}$$

In summary, and with only the non-negligeable terms retained (for the Sentinel-1 orbit examined in this document, κ_0 and τ_0 take on values of approximately 10^{-7}, 10^{-8}, repectively which means that they can be considered negligeable over over a scene of several hundred kilometers in s), one finds that

$$\hat{\mathbf{r}}(s_p)\cdot\mathbf{T}(s_p) = -k_s/k_r \tag{176}$$

$$\hat{\mathbf{r}}(s_p)\cdot\mathbf{N}(s_p) = \cos\phi_0 + \frac{r}{r_0}\sin\phi_0\sin(\phi-\phi_0) \tag{177}$$

$$\hat{\mathbf{r}}(s_p)\cdot\mathbf{B}(s_p) = \sin\phi_0 - \frac{r}{r_0}\cos\phi_0\sin(\phi-\phi_0), \tag{178}$$

which leads the following

$$\begin{aligned}&\alpha_{\parallel_n}k_r\hat{\mathbf{r}}(s_p)\cdot\mathbf{T}(s_p) + k_r\boldsymbol{\alpha}_{\perp n}\cdot[\hat{\mathbf{r}}(s_p)\cdot\mathbf{N}(s_p),\hat{\mathbf{r}}(s_p)\cdot\mathbf{B}(s_p)]\\ &= -\alpha_{\parallel_n}k_s + k_r\boldsymbol{\alpha}_{\perp n}\cdot\hat{\mathbf{r}}_0 + k_r r\frac{\boldsymbol{\alpha}_{\perp n}\cdot\hat{\mathbf{r}}_{0\perp}}{r_0}\sin(\phi-\phi_0)\end{aligned} \tag{179}$$

Note that in the neighbourhood of r_0, ϕ_0, (177) and (178) closely approximate the first order expansion of the cosine and sine functions; thus, in this neighbourhood, one may write

$$\hat{\mathbf{r}}(s_p)\cdot\mathbf{T}(s_p) = -k_s/k_r \tag{180}$$

$$\hat{\mathbf{r}}(s_p)\cdot\mathbf{N}(s_p) = \cos\phi \tag{181}$$

$$\hat{\mathbf{r}}(s_p)\cdot\mathbf{B}(s_p) = \sin\phi \tag{182}$$

In summary, (176), (177), (178), (181), (182) and (50) lead to the following expression for the signal in k-space

$$\mathcal{S}S_n(k_r, k_s) = \mathcal{P}(k_{r'}) e^{i\alpha_{\parallel_n} k_s - ik_r \boldsymbol{\alpha}_{\perp_n} \cdot \hat{\mathbf{r}}_0}$$
$$\int \frac{g(\mathbf{x}) e^{-ik_r r \frac{\boldsymbol{\alpha}_{\perp_n} \cdot \hat{\mathbf{r}}_{0\perp}}{r_0} \sin(\phi - \phi_0)} \mathrm{D}_n[k_r, -k_s/k_r, \cos\phi, \sin\phi]}{r^2(s_p[k_r, k_s])} e^{-ik_r r(s_p[k_r, k_s])} \mathrm{d}\mathbf{x}. \tag{183}$$